RESEARCH ARTICLE

Key Points:
- High-resolution garnet-based P-T paths were estimated for the inverted metamorphic sequence beneath the Himalayan Main Central Thrust (MCT)
- The paths suggest that inverted metamorphism developed due to accretion of MCT footwall slivers
- Paths record evidence for a tectonic pause of the Himalayan MCT (15–8 Ma) and high erosion rates since the Pliocene

Supporting Information:
- Supporting Information S1
- Table S1
- Figure S1
- Table S2

Correspondence to:
E. J. Catlos,
ejcatlos@jsg.utexas.edu

Modeling High-Resolution Pressure-Temperature Paths Across the Himalayan Main Central Thrust (Central Nepal): Implications for the Dynamics of Collision

E. J. Catlos[1] (ID), O. M. Lovera[2] (ID), E. D. Kelly[1,3] (ID), K. T. Ashley[1,4] (ID), T. M. Harrison[2], and T. Etzel[1] (ID)

[1]Department of Geological Sciences, University of Texas at Austin, Austin, TX, USA, [2]Department of Earth and Space Sciences, University of California, Los Angeles, CA, USA, [3]Now at SparkCognition, Austin, TX, USA, [4]Now at Department of Geology and Environmental Science University of Pittsburg, Pittsburgh, PA, USA

Abstract High-resolution, garnet-based pressure-temperature (P-T) paths were obtained for nine rocks across the Himalayan Main Central Thrust (MCT) (Marsyangdi River transect, central Nepal). Paths were created using garnet and whole rock compositions as input parameters into a semiautomated Gibbs free-energy-minimization technique. The conditions recorded by the paths, in general, yield similar T but lower P compared to estimates from mineral equilibria and quartz-in-garnet Raman barometry. The paths are used to modify a model based on a two-dimensional finite difference solution to the diffusion-advection equation. In this model, P-T paths recorded by the footwall garnets result from fault motion at specified times, thermal advection, and alteration of topography. The best fit between the high-resolution P-T paths and model predictions is that from 25 to 18 Ma, samples within the MCT footwall moved at 5 km/Ma, while those in the hanging wall moved at 10 km/Ma. Under these conditions, topography grew to 3.5 km. A pause in activity along the MCT between 18 and 15 Ma allows heat to advect and may be due to a transfer of tectonic activity to the structures closer to the Indian subcontinent. During this time, the topography erodes at a rate of 1.5 km/Ma. Thrusting within the MCT footwall reactivates between 8 and 2 Ma with exhumation rates up to 12 mm/yr since the Pliocene. The results suggest the potential for the highest-resolution garnet-based P-T paths to record both the thermobarometric consequences of fault motion and large-scale erosion.

Plain Language Summary The Main Central Thrust (MCT) is a major Himalayan fault system largely responsible for the generation of its high topography. Garnets across the MCT record their growth history in the crust through changes in their chemistry. These chemical changes can be extracted and modeled. Here we report detailed pressure-temperature paths recorded by garnets collected across the MCT along the Marsyangdi River in central Nepal. The paths track evolving conditions in the Earth's crust when the MCT was active during the growth of the Himalayas. The results suggest that the MCT formed as individual rock packages moved at distinct times. Further modeling makes predictions about how the Himalayas developed, including that the MCT may have ceased motion 18–15 million years ago, as other faults closer to the Indian subcontinent became active, and that it reactivated 8–2 million years ago, leading to the generation of high topography. The modeling also suggests that very high erosion rates occurred within the range after reactivation. Although garnets have long been used to understand how fault systems evolve, we provide details of an approach that allows higher-resolution data to be extracted from them and show how they could be used to track large-scale erosion.

1. Introduction

Tectonic models as a universal outcome generate predictions regarding the traveltime paths of rocks as they are displaced due to the application of particular input parameters and boundary conditions. A need for most of these models, either as a constraint for realistic input conditions or to gauge their relevance to a particular natural system, is pressure-temperature-time (P-T-t) paths from individual rock samples that track the conditions they experienced during displacement. Although arguments can be made that P-T paths and absolute peak P-T conditions may not necessarily be diagnostic of processes involved (e.g., Gervais & Brown, 2011), this type of information is clearly a valuable addition to other types of data, such as timing and microstructural information regarding strain recorded during rock deformation (see Kohn, 2016; Rolfo et al., 2014).
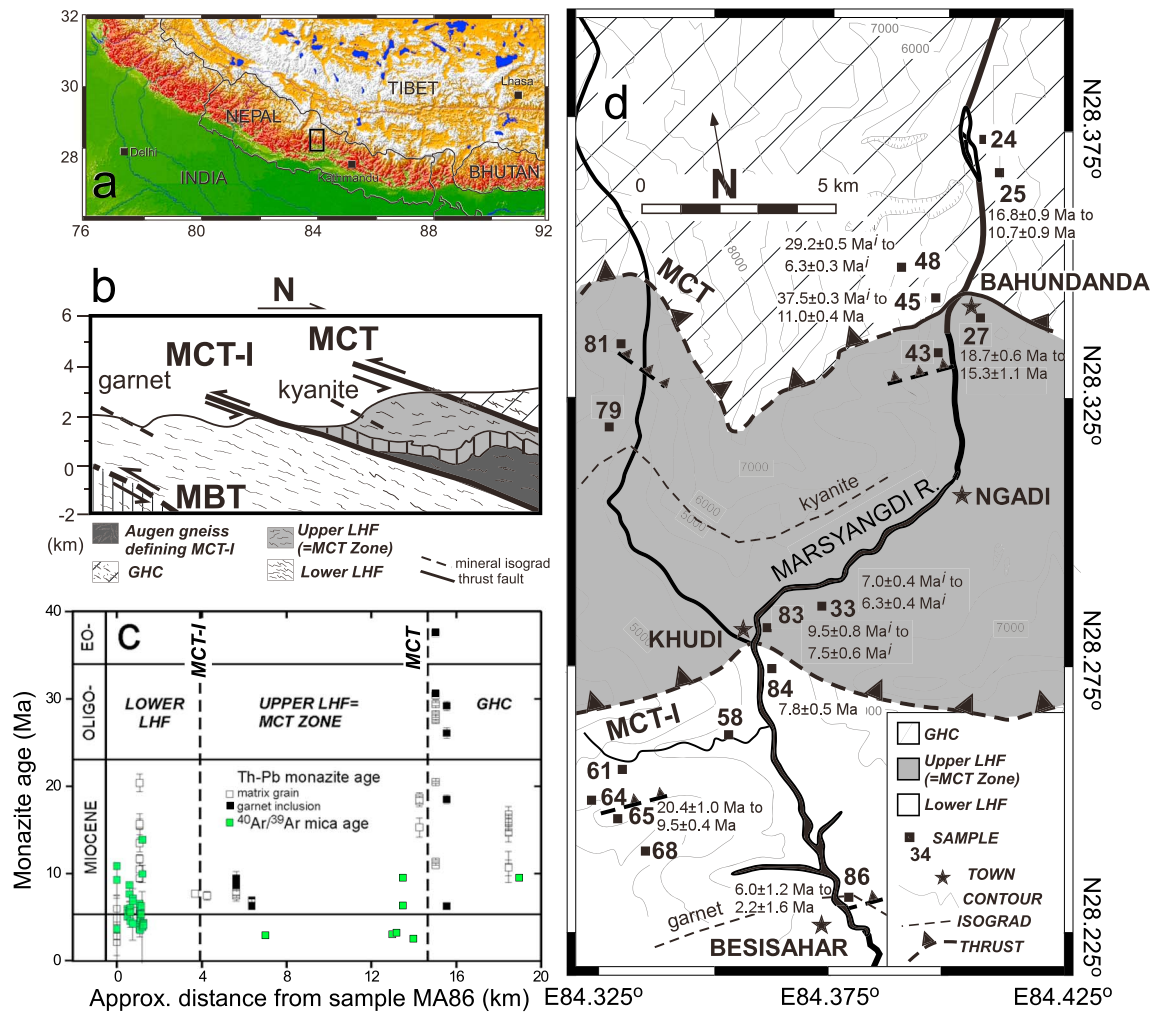
Figure 1. Figures summarize the location and previous work generated for rocks analyzed in this study. (a) ArcGIS map of the Himalayas showing the location of the field area. (b) Cartoon cross section across the MCT shear zone (after Catlos et al., 2001). MCT = Main Central Thrust, MBT = Main Boundary Thrust. (c) A plot of monazite and $^{40}Ar/^{39}Ar$ mica age versus approximate distance from sample MA86. Data include those reported in Edwards (1995) from the same transect. GHC = Greater Himalayan Crystallines, LHF = Lesser Himalayan Formations. (d) Sample location map. Sample locations and range of monazite ages ($\pm 1\sigma$) are indicated. Ages reported in Catlos et al. (2001).

Zoned garnets have long been used to generate P-T paths (e.g., George & Gaidies, 2017; Goscombe & Hand, 2000; Imayama et al., 2010; Larson et al., 2013; Moynihan & Pattison, 2013; Spear & Selverstone, 1983; Spear et al., 1990; Wang et al., 2016). However, low-resolution P-T paths can be limited in their ability to test ideas regarding lithospheric response to perturbations, including motion within fault zones. Here we apply advances in thermodynamic modeling (de Capitani & Petrakakis, 2010; Moynihan & Pattison, 2013) to acquire high-resolution P-T paths that show the conditions responsible for garnet growth within one of the Himalayas' major fault systems. The paths are used to first test the predictions of a shear zone imbrication model (Harrison et al., 1998) and then to modify the model's parameters to best fit conditions recorded by its garnets. The approach we outline can be applied to any garnet-bearing assemblage using easily obtained information (bulk rock and mineral compositions) and have the potential to significantly increase the understanding of the dynamics of field areas that contain garnet, from the mineral's crystallization to erosion-driven or tectonically driven exhumation.

2. Geological Background: Himalayan Case Study

The Main Central Thrust (MCT; Figure 1) plays a central role in many models for the evolution of the Himalayas (e.g., Bollinger et al., 2006; Carosi et al., 2013; England et al., 1992; Harrison et al., 1998; Henry et al., 1997;

AGU
100
ADVANCING EARTH
AND SPACE SCIENCE

Tectonics

10.1029/2018TC005144

Le Fort, 1975; Martin, 2017; Parsons et al., 2016; Searle & Rex, 1989, among others). The MCT places the high-grade (>600 °C) Greater Himalayan Crystallines (GHCs) over lower grade Lesser Himalayan Formations (LHFs) along a broad scale 8–12-km thick shear zone (see review in Mukhopadhyay et al., 2017). The MCT foot-wall is characterized and defined by inverted metamorphism, where metamorphic grade increases toward structurally shallower levels (e.g., Chakraborty et al., 2016; Larson et al., 2015; Pêcher, 1989; Searle et al., 2008). Pressure-temperature (P-T) conditions and paths obtained from garnet-bearing assemblages from the shear zone have long been applied to decipher the origin of this apparent inverted metamorphism (Anczkiewicz et al., 2014; Imayama et al., 2010; Kaneko, 1995; Larson et al., 2013; Metcalfe, 1993; Manickavasagam et al., 1999; Mottram et al., 2014; Staeubli, 1989; Vannay & Hodges, 1996; Vannay & Grasemann, 1998).

A wide range of explanations have been proposed: from multiple episodes of imbrication and deformation in the MCT footwall (Caddick et al., 2007; Catlos et al., 2001; Groppo et al., 2009,2010; Herman et al., 2010; Mosca et al., 2012; Mottram, Argles, et al., 2014; Mottram, Warren, et al., 2014) to the alternative end-member of tectonic inversion of a coherent rock package that experienced a single Barrovian metamorphism event (Gaidies et al., 2015; Hubbard, 1996; Martin et al., 2010). The hot iron model, in which the primary source of heat for the inverted metamorphic sequence is thermal energy from the GHC due to the emplacement along the MCT (England & Molnar, 1993), has its alternative, end-member, where no contribution of dissipative to downward conductive heating from the GHC was required (Stephenson et al., 2000). Other explanations include multiple episodes of ductile overthrusting of the GHC over the LHF (Goscombe & Hand, 2000), post and tectonic overpressure that changed fundamental rock properties and facilitated its development (Thakur et al., 2015; model of Schmalholz & Podladchikov, 2013).

A more recent trend is the redelegation of models once exclusively dedicated to describing the tectonic evolution of the MCT hanging wall to its footwall. For example, channel flow was originally conceived as the extrusion of the GHC due to synchronous activity along the MCT and a structurally higher South Tibetan Detachment System (STDS) with focused erosion along the topographic front (e.g., Beaumont et al., 2001; Cottle et al., 2015; Long & McQuarrie, 2010). In this modified scenario, the inverted metamorphic sequence tectonically exhumes along discrete fault systems within the LHF and the MCT or other faults within the GHC during the Miocene (Goswami-Banerjee et al., 2014; Imayama et al., 2010). Goswami-Banerjee et al. (2014) suggest that LHF channel flow was episodic and followed by imbrication as the unit experienced deformation to attain a critical taper (Kohn, 2008). Alternatively, Daniel et al. (2003) suggest that inverted metamorphism is an outcome of channel flow experienced by the GHC. The process of large-scale folding that aligns preexisting isograds into an apparent inverted metamorphic position was also initially attributed to the development of the GHC (Searle & Rex, 1989). This is now also used to describe a large-scale fold and metamorphism observed in the LHF at its NE syntaxis (Nandini & Thakur, 2011).

Overall, models for Himalayan inverted metamorphism have broadened our understanding of how heat and mass flow can evolve during collisional processes, but their applicability to the range is a subject of debate (e.g., Ambrose et al., 2015; Beaumont et al., 2001; Harrison et al., 1998; Hodges, 2006; Kohn, 2008). The range of options suggest that more detailed, higher-resolution constraints from the rocks themselves are needed. We note that some workers report P-T conditions from the MCT inverted metamorphic sequence with no pre-ferred model due to the limited nature of the data sets with which to interpret geodynamics (Goswami et al., 2009) or report conditions consistent with multiple interpretations (Rapa et al., 2016).

Here we apply new thermodynamic approaches to Himalayan assemblages across the MCT that contain gar-nets preserving prograde compositions. The results provide insight into the dynamics of Himalayan uplift and suggest possibilities regarding episodic motion within the range and the potential for garnet-based thermo-barometry to record large-scale erosion. The samples were collected along the Marsyangdi River (Nepal) sec-tion of the MCT (Figure 1) and have been well characterized previously, with monazite Th-Pb and mica $^{40}Ar/^{39}Ar$ age data and P-T estimates obtained via mineral equilibria ("conventional" approaches; Table 1; Catlos et al., 2001). The goal is to generate the highest-resolution P-T paths possible from their garnets to document conditions of crystal growth from center to rim using a thermodynamic modeling routine (Moynihan & Pattison, 2013). In addition to nine new high-resolution P-T paths, we report new P estimates using quartz-in-garnet (QuiG) Raman barometry (Ashley, Caddick, et al., 2014; Ashley, Steele-MacInnis, et al., 2014; Kohn, 2014a) from six samples. The P-T paths are then evaluated in the context of the Harrison et al. (1998) thermal model for the evolution of the Himalayan region from 25 to 2 Ma.

Table 1
Summary of P-T Conditions of Samples Analyzed

Sample[a]	GBT (°C)[b]	GPBMP (kbar)[c]	T-D coreT (°C)[d]	T-D coreP (kbar)[e]	T-D rimT (°C)[f]	T-D rimP (kbar)[g]	QuiGP (kbar; at T[°C])[h]
Greater Himalaya Crystallines							
MA24	600 ± 18	9.32 ± 0.37	580 ± 50	8.65 ± 1.20	640 ± 7	8.60 ± 28	n.m.
MA45	745 ± 20	11.50 ± 0.50	n.m.[i]	n.m.	n.m.	n.m.	6.81 ± 0.50 (550 °C)
Upper Lesser Himalaya Formation							
MA27	635 ± 20	7.80 ± 1.00	n.m.	n.m.	n.m.	n.m.	n.m.
MA43	650 ± 20	8.78 ± 0.74	490 ± 3	4.75 ± 0.25	553 ± 4	4.58 ± 0.25	6.87 ± 0.80 (500 °C)[j]
							6.15 ± 0.43 (560 °C)
MA79	523 ± 53	n.m.	544 ± 6	5.70 ± 0.28	573 ± 4	6.63 ± 0.18	6.44 ± 0.53 (550 °C)
MA33	565 ± 15	6.50 ± 0.50	n.m.	n.m.	n.m.	n.m.	6.57 ± 0.42 (540 °C)
MA83	550 ± 25	n.m.	n.m.	n.m.	n.m.	n.m.	n.m.
Lower Lesser Himalaya Formation							
MA58	508 ± 38	n.m.	533 ± 4	4.20 ± 0.28	560 ± 7	5.00 ± 0.42	n.m.
MA61	550 ± 25	8.26 ± 0.58	523 ± 4	6.18 ± 0.18	557 ± 5	6.75 ± 0.21	7.92 ± 56 (535 °C)
MA64	475 ± 35	n.m.	525 ± 1	4.25 ± 0.21	555 ± 2	4.38 ± 0.25	n.m.
MA65	525 ± 30	7.34 ± 0.90	535 ± 4	4.20 ± 0.28	554 ± 6	4.50 ± 0.14	7.08 ± 0.60 (550 °C)
MA68	513 ± 38	n.m.	538 ± 4	3.83 ± 0.39	565 ± 10	>5	n.m.
MA86	530 ± 25	6.98 ± 0.64	547 ± 5	5.05 ± 0.21	568 ± 4	5.20 ± 0.28	n.m.

[a]Samples are arranged in order from hanging wall to structurally lowest. [b]Temperatures determined using garnet-biotite (GB) thermometry (Berman, 1990; Ferry & Spear, 1978) with uncertainty representing the range of conditions at the specified pressures. If no P was measured, these temperatures represent the conditions from 0 to 10,000 bars (from Catlos et al., 2001). Other thermometers could be applied and reestimated, but we report these conditions as the thermal-kinematic model discussed that relied on these conditions for development. [c]Pressures determined using garnet-plagioclase-biotite-muscovite (GPBM) barometry (Hoisch, 1990; from Catlos et al., 2001). Other barometers could be applied and reestimated, but we report these conditions as the thermal-kinematic model discussed that relied on these conditions for development. [d]Temperature estimate for the core of the garnet using Theriak-Domino. [e]Pressure estimate for the core of the garnet using Theriak-Domino. [f]Temperature estimate for the rim of the garnet using Theriak-Domino. [g]Pressure estimate for the core of the garnet using Theriak-Domino. [h]Quartz inclusion in garnet P conditions at a specified T. Four inclusions were measured in sample MA61, three in sample MA33 and MA43 (core), two in samples MA65, MA79, and MA43 (rim), and one in sample MA45. [i]Abbreviation n.m. = not measured. [j]The first value is for three inclusions in the core, and second value is average of two values in the garnet rim.

3. Materials and Methods

3.1. Sampling and Previous Results

We report new P-T data from 13 garnet-bearing, Al-rich metapelites collected across the MCT along the Marsyangdi River drainage in central Nepal (sample number MA-#, Figure 1 and Table 1). Mineral compositional data, X-ray element maps of the analyzed garnets and modeling results are available in the supporting information.

Catlos et al. (2001) defined the upper LHF (= MCT shear zone) rocks as those collected between the MCT and MCT-I. The MCT-I (Figure 1b) was originally considered as the base of the upper LHF documented by the appearance of an augen gneiss (see Arita, 1983) and may have its equivalents across the Himalayan range (i.e., the Munsiari Thrust; see Moharana et al., 2013). The presence of the MCT-I in the Marsyangdi area is debated because the boundary separating upper and lower Lesser Himalayan metasediments is unclear (see Upreti, 1999). The MCT-I is assigned here as the contact between aluminous and carbonate schists of the upper LHF and similar rocks of the Kunchha Formation and is characterized by garnet-bearing rocks with late Miocene monazite inclusions (Figure 1c). Catlos et al. (2001) delegate lower LHF samples below the MCT-I.

All samples have garnet + biotite ± plagioclase + muscovite + quartz with accessory minerals monazite, tourmaline, rutile, and/or ilmenite. Sample MA79 also contains graphite. In situ (dated in thin section) Th-Pb monazite ages have been reported for nine of the rocks (Figure 1c; Catlos et al., 2001). P-T conditions were previously ascertained using garnet-biotite (GB) thermometry (all samples; Berman, 1990; Ferry & Spear, 1978) and garnet-plagioclase-biotite-muscovite (GPBM) barometry (n = 8 rocks; Hoisch, 1990). In some samples, plagioclase was not found, so only a maximum T was estimated. P-T paths were previously generated for three rocks using the methods outlined in Spear and Selverstone (1983) and Spear (1993). All previous data are described in detail in Catlos (2000) and Catlos et al. (2001), with monazite ages summarized in Figure 1c and P-T conditions reported in Table 1. Some of these ages have also been the focus of textural analysis and interpretation (Kohn, 2016).

Samples MA24, MA25, MA48, and MA45 are from the GHC (Figure1). Sample MA24 is the only rock from the unit that was appropriate for high-resolution P-T path modeling using the approach outlined here. MA24 has large garnets (~2 mm in diameter) and is the least affected by diffusional modification compared to adjacent samples with smaller garnets that were significantly affected by this process. A number of researchers have targeted of garnet-based P-T estimates from diffusion-modified GHC mineral assemblages (Carosi et al., 1999; Corrie & Kohn, 2011; Coleman, 1998; Fraser et al., 2000; Guillot, 1999; Hodges et al., 1988, 1996; Hubbard, 1989; Imayama et al., 2010; Inger & Harris, 1992; Kohn, 2008; Lombardo & Rolfo, 2000; Macfarlane, 1995; Martin et al., 2010; Metcalfe, 1993; Montomoli et al., 2013; Pognante & Benna, 1993; Vannay & Hodges, 1996; Wang et al., 2016). This unit has experienced high T (>600 °C), which leads to modification of prograde garnet compositions and increases the potential for erroneous estimates through retrograde reactions (Kohn & Spear, 2000). Diffusion that affects an entire garnet grain makes it challenging to make meaningful assumptions about its prograde history (e.g., Spear, 1993). Although garnet in sample MA24 does not contain quartz inclusions for QuiG barometry, garnet in structurally lower sample MA45 has one appropriate for the approach (Table 1). GHC garnets analyzed that near-sample MA24 have monazite inclusions that are Eocene, early Miocene, and late Miocene, and matrix grains that are early to late Miocene (Figure 1c; Catlos et al., 2001).

Five rocks were collected from upper (MA27, MA43, and MA79) and lower (MA33 and MA83) bounds of the mapped MCT shear zone. Only Upper LHF samples MA43 and MA79 have garnets with zoning profiles suitable for P-T path modeling. Garnets in sample MA27 show evidence of diffusional modification, and those in MA33 have large changes in compositional zoning at the midrim (see Figure 3 and Plate 7 in Catlos et al., 2001). Significant changes in zoning could be attributed to a major modification in rock bulk composition, a process unable to be accommodated using the P-T modeling approach applied here. We report QuiG pressures for MA33 (n = 3 near center), MA79 (n = 2 near center), and MA43 (n = 3 near center and n = 2 near rim; Table 1). Monazite grains were dated samples MA27, MA33, and MA83 previously and are early to late Miocene (Figure 1c).

Seven samples were collected from the lower LHF (MA84, MA58, MA61, MA64, MA65, MA68, and MA86). All of these rocks were subjected to the P-T modeling approach, except sample MA84. This rock and sample MA65 contain late Miocene monazite (Figure 1c). However, a matrix monazite in sample MA65 is early Miocene. Sample MA86 is the structurally lowest rock analyzed and yields monazite Th-Pb ages that range from 6.0 ± 1.2 Ma to 2.2 ± 1.6 Ma. The considerable uncertainty is because the grains are so young that radiogenic Pb was difficult to measure (Catlos et al., 2001). Martin et al. (2014) place a thrust fault at this location. Two quartz inclusions in garnet from sample MA68 and four in sample MA61 were analyzed for QuiG barometry (Table 1). The other rocks did not have quartz grains suitable for the approach.

3.2. Modeling Garnet Core and Rim P-T Conditions and Paths

Using rock bulk compositions (Tables 2–4), garnet crystal chemistry (Catlos et al., 2001), and the automated routine of Moynihan and Pattison (2013), P-T paths are constructed for samples from the GHC (MA24), upper (MA43 and MA79), and lower LHF (MA58, MA61, MA64, MA65, MA68, and MA86).

In the first step of this approach, an isochemical phase diagram is created for each sample using rock bulk compositions, the software package Theriak-Domino (de Capitani & Brown, 1987; de Capitani & Petrakakis, 2010) with the Holland and Powell (1998 with updates to solution models through 2010) thermodynamic data set, and appropriate mixing models in the system $MnO–Na_2O–CaO–K_2O–FeO–MgO–Al_2O_3–SiO_2–H_2O–TiO_2$ (Table 2 and Figure 2). The specific solid solution models called on in this study are feldspar (Baldwin et al., 2005; Holland & Powell, 2003), garnet (Mahar et al., 1997; White et al., 2000, 2005; Zeh & Holness, 2003), biotite (Powell & Holland, 1999; White et al., 2000), white mica (Coggon & Holland, 2002), ilmenite (Ideal Mn-Mg-Fe solution), chlorite (Holland et al., 1998), staurolite (Holland & Powell, 1998; Mahar et al., 1997), and chloritoid (Mahar et al., 1997; White et al., 2000). The system was considered to form in the presence of water (activity of H_2O = 1.0), and the iron oxidation state was 2+.

In the next step of the process, isopleths of ±0.01 mole fraction spessartine, almandine, pyrope, grossular, and ±0.01 Mg-# (Mg/Fe + Mg), corresponding with the garnet core composition, are plotted on the phase diagram. This initial isochemical phase diagram with intersecting garnet isopleths approximates the chemical system at the time garnet began growth (Figure 2). This diagram also serves to test if the thermodynamic data set and mixing models used in the modeling are appropriate for these particular samples, as

Table 2

Bulk Compositional Data (mol%) Used for Generating the Phase Diagrams Seen in Figure 2

Sample	MA24[a]	MA43[a]	MA61[a]	MA86[a]	MA64[b]	MA68[b]	MA65[c]	MA58[d]	MA79[d]
SiO_2	59.359	60.700	65.963	61.821	59.105	56.591	80.154(0.40)	57.353(0.30)	50.571(0.70)
Al_2O_3	19.280	23.293	15.997	20.982	25.841	26.988	9.337(0.27)	25.190(0.20)	20.115(0.47)
Fe_2O_3	5.252	5.439	5.067	4.313	4.654	5.429	2.535(0.26)	4.657(0.18)	7.816(0.27)
MnO	0.065	0.107	0.057	0.041	0.073	0.098	0.024(0.06)	0.033(0.06)	0.105(0.25)
MgO	5.686	1.759	3.245	2.872	3.044	2.958	1.463(0.02)	2.347(0.01)	7.876(0.02)
CaO	0.963	0.429	1.569	0.310	0.124	0.299	0.441(0.03)	0.383(0.05)	4.028(0.16)
Na_2O	2.836	2.610	3.978	1.419	1.307	1.233	0.579	1.249	3.100
K_2O	5.879	5.077	3.588	6.157	7.115	7.250	2.003	7.508	4.842
TiO_2	0.518	0.528	0.413	0.420	0.362	0.471	0.217	0.396	0.580
P_2O_5	0.162	0.058	0.122	0.098	0.098	0.090	0.228	0.091	0.073

[a]Data generated using FUS-ICP methods.   [b]Data generated using XRF methods.   [c]Data generated using XRF methods but is lower than the original values as indicated by the number in parentheses. Na_2O, K_2O, TiO_2, and P_2O_5 are not affected.   [d]Data generated using FUS-ICP methods but is lower than the original values as indicated by the number in parentheses. Na_2O, K_2O, TiO_2, and P_2O_5 are not affected.

expected mineral assemblages appeared in the phase diagrams with intersecting core isopleths. Changing the parameters alters these observations and result in a model failure.

The garnet "core" is identified as having the highest Mn content and located near a central portion of the mineral. Although we likely did not measure the real garnet core due to the sectioning of the sample, most of the garnet core conditions lie near the 1% volume garnet growth contour (Figure 2; see discussion in section 6.1). Garnet compositions were obtained using an electron microprobe at transects across grains at 20-μm spacing and were evaluated to ensure that they fit stoichiometry (Figures 3–5; see Catlos et al., 2001 for details regarding operational conditions). Transects from core to rim were made across garnets in MA24, MA65, and MA86, and complete transects were done edge to edge across garnets in all other samples. We also obtained additional core-rim transects across garnets in samples MA61 and MA43. Each transect is used to generate individual P-T paths.

After the garnet core conditions are estimated, we use a Matlab script to apply the Theriak-Domino program (de Capitani & Brown, 1987; de Capitani & Petrakakis, 2010) to search the P-T grid for the smallest misfit between the modeled garnet and measured composition and then calculate the portion of the bulk composition sequestered in the first step of garnet growth. Sequestered components are subtracted from the original rock bulk composition to estimate an "effective" bulk composition for the next step of garnet growth. The process is repeated for all data points along a garnet zoning profile from core to rim. Each step along a garnet traverse yields both an estimate of the P-T conditions of incremental growth and a new effective bulk rock composition, ultimately culminating in a P-T path (Figures 6 and 7).

Once the path is generated, the final step is to create a phase diagram using the last estimated effective bulk composition (Tables 3 and 4) and garnet rim composition. In some cases, isopleths of ±0.01 An content [Ca/(Ca + Na + K)] from matrix plagioclase (sample MA24, Figure 6) or ±0.01 Mg-# (Mg/Mg + Fe) from matrix biotite (samples MA58, MA64, MA61, and MA65, Figure 7) are overlaid on the rim phase diagrams. Matrix mineral compositions from these rocks were the only to yield conditions that overlap or lie near those corresponding to the garnet rim.

Six samples (MA33, MA43, MA45, MA61, MA65, and MA79) have inclusions suitable for QuiG barometry (Table 1). The barometer is largely independent of thermodynamic calculations and can be used to compare to the P conditions suggested by the Theriak-Domino approach. Inclusion and formation pressures were determined for these samples using the pressure-sensitive Raman wave shift calibration for the ν464 band (Ashley et al., 2014) and the modeling approach of Ashley et al. (2015). QuiG barometry shows promise for obtaining accurate and precise

Table 3

Effective Bulk Compositional Data (mol%) Used for Generating Final Phase Diagrams for Greater Himalayan Crystallines (MA24) and MCT Shear Zone (MA43 and MA79) Samples

	MA24	MA43 Path 1[a]	MA43 Path 2	MA43 Path 3	MA79 Path 1[a]	MA79 Path 2
SiO_2	57.218	59.368	59.054	58.998	49.586	49.488
Al_2O_3	17.853	22.405	22.196	22.158	19.459	19.393
Fe_2O_3	3.777	4.449	4.176	4.143	7.210	7.140
MnO	5.410	1.718	1.700	1.699	7.808	7.799
MgO	0.002	0.001	0.000	0.002	0.011	0.009
CaO	0.636	0.234	0.211	0.188	3.811	3.794
Na_2O	2.836	2.610	2.610	2.610	3.100	3.100
K_2O	5.879	5.077	5.077	5.077	4.842	4.842
TiO_2	0.518	0.528	0.528	0.528	0.580	0.580

[a]Data are generated by the Theriak-Domino program at the final step of the P-T path and represent the effective bulk composition recorded near the garnet rim. The compositions for Path 1 are used to generate the phase diagrams. See Figure 6 for phase diagrams.

AGU
100
ADVANCING EARTH
AND SPACE SCIENCE

Tectonics

10.1029/2018TC005144

Table 4
Effective Bulk Compositional Data (mol%) Used for Generating the Phase Diagrams for Lower Lesser Himalaya Formation Samples

	MA58D Path 1[a]	MA58D Path 2	MA61Path 1[a]	MA61 Path 2	MA61 Path 3	MA64 Path 1[a]	MA64 Path 2	MA65	MA68 Path 1[a]	MA68 Path 2	MA86
SiO_2	56.674	56.483	65.412	65.294	65.205	58.751	58.909	79.764	54.969	55.042	61.402
Al_2O_3	24.738	24.610	15.630	15.551	15.491	25.605	25.710	9.077	25.907	25.956	20.702
Fe_2O_3	4.151	3.995	4.709	4.621	4.559	4.418	4.531	2.230	4.262	4.313	4.020
MnO	2.313	2.299	3.221	3.214	3.210	3.025	3.035	1.438	2.868	2.867	2.848
MgO	0.002	0.001	0.009	0.005	0.004	0.020	0.038	0.006	0.003	0.004	0.009
CaO	0.276	0.256	1.448	1.429	1.407	0.078	0.095	0.369	0.094	0.116	0.240
Na_2O	1.249	1.249	3.978	3.978	3.978	1.307	1.307	0.579	1.233	1.233	1.419
K_2O	7.508	7.508	3.588	3.588	3.588	7.115	7.115	2.003	7.250	7.250	6.157
TiO_2	0.396	0.396	0.413	0.413	0.413	0.362	0.362	0.217	0.471	0.471	0.420

[a]Data are generated by the Theriak-Domino program at the final step of the P-T path and represent the effective bulk composition recorded near the garnet rim. The compositions for Path 1 are used to generate the phase diagrams in Figure 7.

pressures from garnet, even those within altered or retrograde metamorphosed rocks (e.g., Ashley, Caddick, et al., 2014; Ashley, Steele-MacInnis, et al., 2014, 2016; Kohn, 2014b; Spear et al., 2014). The baric estimates are reported for thermal conditions indicated in Table 1 and are plotted in Figures 6 and 7. The predictions of the Theriak-Domino paths are also compared to previous P-T conditions and paths reported for these samples (Catlos et al., 2001).

4. Data

Two sources of raw data are needed for the modeling approach: mineral and bulk-rock compositions. To increase the number of data points used to construct the highest-resolution P-T paths possible, we apply a Savitzky-Golay smoothing function to transects in spessartine, grossular, almandine, and pyrope compositions across garnet and use the smoothed data to generate a P-T path (Figures 3–5). This approach assumes that no significant changes in chemistry exist in the garnets where no data are observed and that closely spaced variations in chemistry are the result of typical error and uncertainty in electron microprobe analysis (e.g., imperfect polish and counting statistics). The use of the smoothed path allows conditions to be estimated across gaps that occur due to lack of measurement, cracks, or inclusions. Also, the approach helps to maintain computational stability and faster fits with the Nelder-Mead search routine of the program. Paths from garnets with major changes in composition over short distances (i.e., sample MA33; Catlos et al., 2001) are unable to be modeled using the approach, and likely should not be, as they may be the result of changes in bulk rock composition and/or significant changes in P-T conditions that are unable to be accommodated using the program. After the Theriak-Domino approach was applied to create the P-T path, we compare the predicted garnet compositional zoning to both the original and smoothed compositions. If significant discrepancies appeared (>0.1-mole fraction for spessartine, grossular, almandine, and pyrope contents), we adjusted the P-T conditions (±1–5 °C, ±100–200 bars) and retained the best fit.

In six samples (MA43, MA58, MA61, MA64, MA68, and MA79), we generate two or three P-T paths to gauge reproducibility (Figures 4 and 5). In these cases, rim to rim compositions (two core-rim profiles) or additional garnets from the same sample were analyzed using the sample analytical conditions and during the same analytical session. Multiple paths are helpful in ensuring that we approach the garnet core and initial growth conditions, as ultimately, without confirmation and analysis of the real garnet core and rim, the paths record only a portion of the overall garnet growth history.

The transects are also useful to show how minor changes in shape and location of the P-T paths affect a best fit match between modeled and either smoothed or electron microprobe garnet compositions. For example, Path 1 for a garnet in sample MA79 appears to fit the grossular, almandine, and pyrope compositional data better than Path 2 (Figures 4e–4h). However, the P-T paths generated for both transects are similar in their shape and location in P-T space (Figure 6b). The analysis of multiple paths also allows evaluation of divergence between the fit of modeled data and garnet compositions that appear at consistent locations within
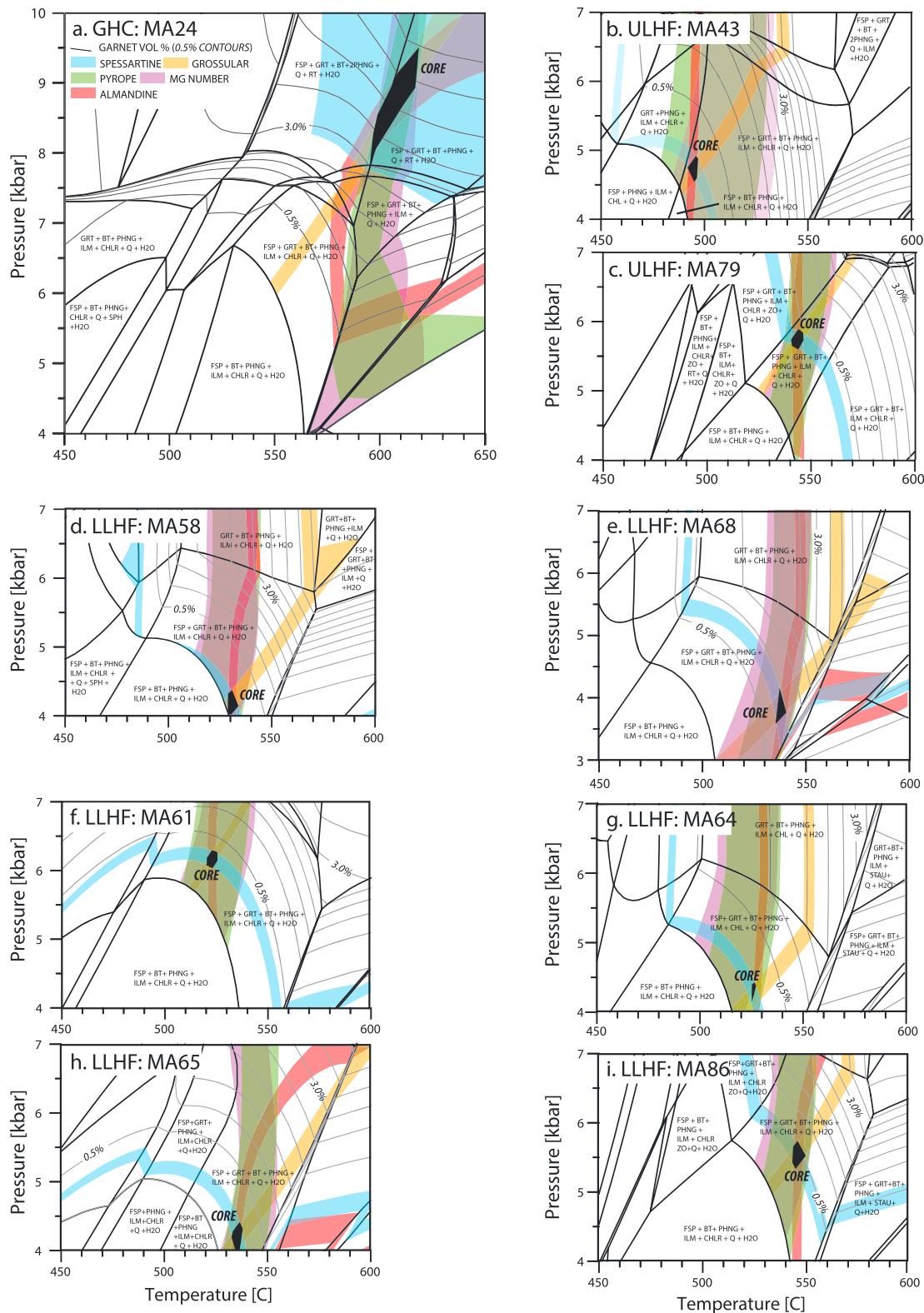
Figure 2. Isochemical phase diagrams for each sample using the rock bulk compositions in Table 2. See Figure 1 for sample locations. Abbreviations: GHC = Greater Himalayan Crystallines; ULHF=Upper Lesser Himalaya Formation, LLHF = Lower Lesser Himalayan Formation. (a–i) Fields of mineral assemblages and sample names are labeled in each panel. Overlain on each diagram are lines of garnet volume in 0.5% contours and garnet core isopleths (±0.1 mole fraction or ± 0.1 Mg-#; colored regions). Garnet core P-T conditions are where isopleths of spessartine, grossular, pyrope, Mg-#, and almandine intersect and is indicated by a black polygon. Mineral abbreviations after de Capitani and Brown (1987) and de Capitani and Petrakakis (2010), and PHG = muscovite.
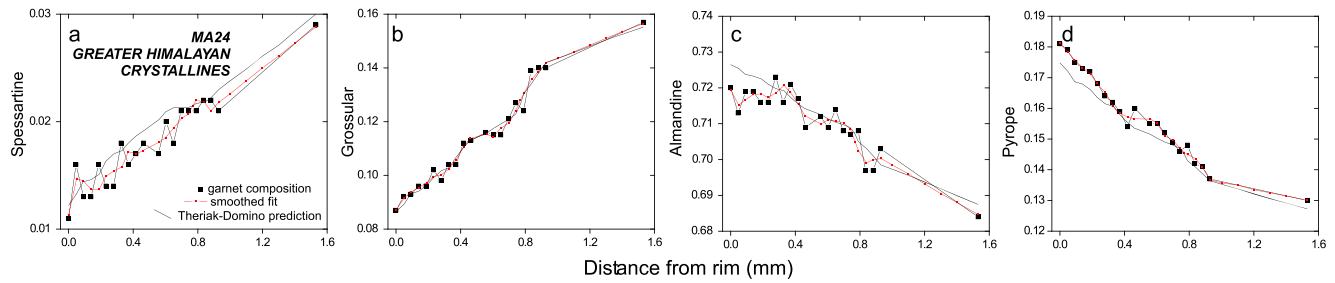
Figure 3. Compositional transect across garnet in sample MA24 in (a) spessartine, (b) grossular, (c) almandine, and (d) pyrope. Black squares are the garnet composition obtained using an electron microprobe. Red lines show the smoothed fit of the electron microprobe data and are compositions used in the modeling program. Smoothing helps to maintain computational stability and faster fits with the Nelder-Mead search routine of the program (see discussion in section 4). The black line is the model-predicted garnet zoning.
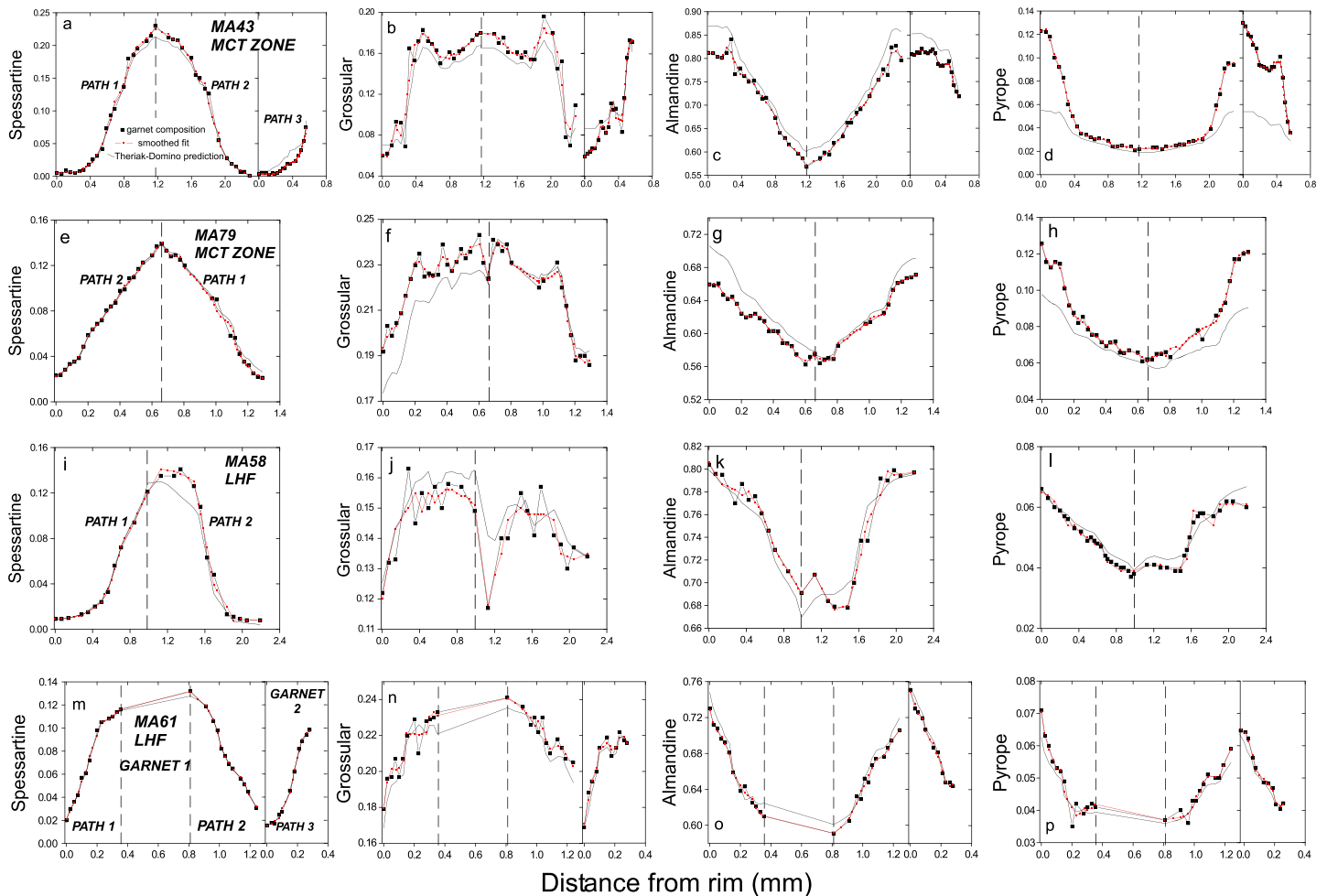
Figure 4. Transects across garnets in upper (MCT shear zone) and lower Lesser Himalaya Formation (LHF), comparing garnet spessartine, grossular, almandine, and pyrope compositions, smoothed fit, and Theriak-Domino model predictions. Data from sample MA43 are seen in panels (a–d) and MA79 in panels (e–h). Data from sample MA58 is presented in panels (i–l), and MA61 is shown in panels (m–p). Black squares are the garnet composition obtained using an electron microprobe. Red lines are the smoothed fit of the data and are used in the modeling program. The black lines are the model-predicted garnet zoning. Paths are numbered. In sample MA61, Path 3 is along a different garnet than Paths 1 and 2. In sample MA43, all paths are taken from the same garnet.
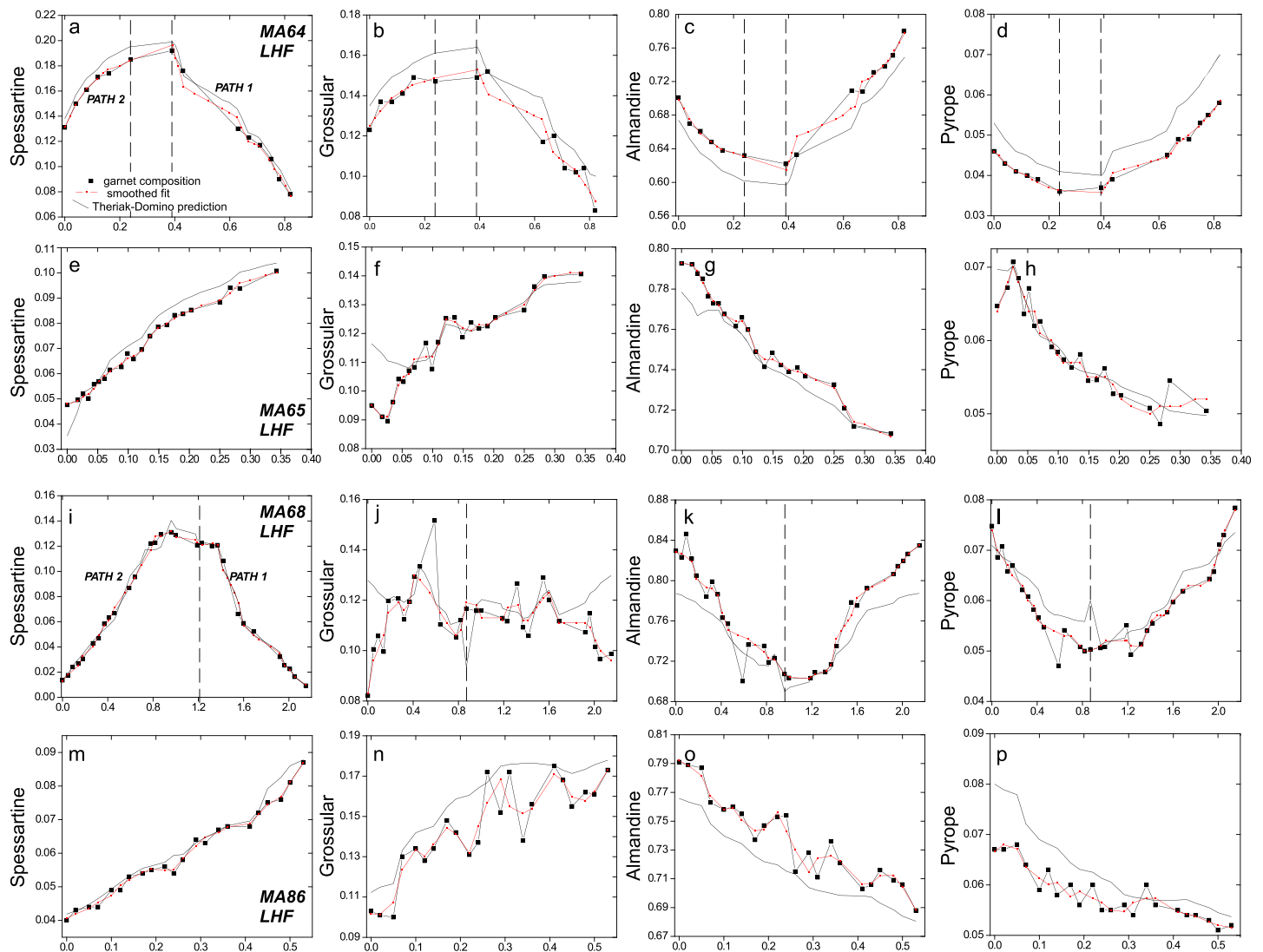
Figure 5. Transects across garnets from the LHF, comparing garnet spessartine, grossular, almandine, and pyrope compositional data, smoothed fit, and Theriak-Domino model predictions. Data from sample MA64 are seen in panels (a–d), MA65 in (e–h), MA68 in (i–l), and MA86 in (m–p). Black squares are the garnet composition obtained using an electron microprobe. The red line is the smoothed fit of the data and those used in the modeling program. The black line is the model-predicted garnet zoning. Paths are numbered.

a garnet. For example, in sample MA43, the grossular, pyrope, and almandine contents suggested by the modeling approach consistently diverge from the smoothed and electron microprobe garnet compositions at 0.5 mm of the garnet rim (Figures 4b–4d). This observation is consistent with all three of the garnet transects.

Whole rock bulk compositions are the primary data used to generate the core phase diagrams (Table 2). The major element data for samples MA24, MA43, MA58, MA79, MA61, and MA86 were obtained using fusion inductively coupled plasma mass spectrometry (FUS-ICP, Activation Laboratories; ±0.1% detection limits). These data for samples MA64, MA65, and MA68 were obtained using X-ray fluorescence procedures (XRF, Franklin and Marshall College, ±0.1% detection limits, FeO analyzed via titration). Samples are medium-grained pelites; thus, using this type of bulk composition for generating the isochemical phase diagrams is likely suitable (Tinkham & Ghent, 2005). Initial phase diagrams using the data for samples MA58, MA65, and MA79 produced garnet-in reactions at low P-T conditions (<3 kbar, <300 °C). The bulk composition of the samples combined with the composition of the garnet core will strongly influence the first appearance of garnet growth and, in some cases, can predict the presence of garnet at lower conditions than is
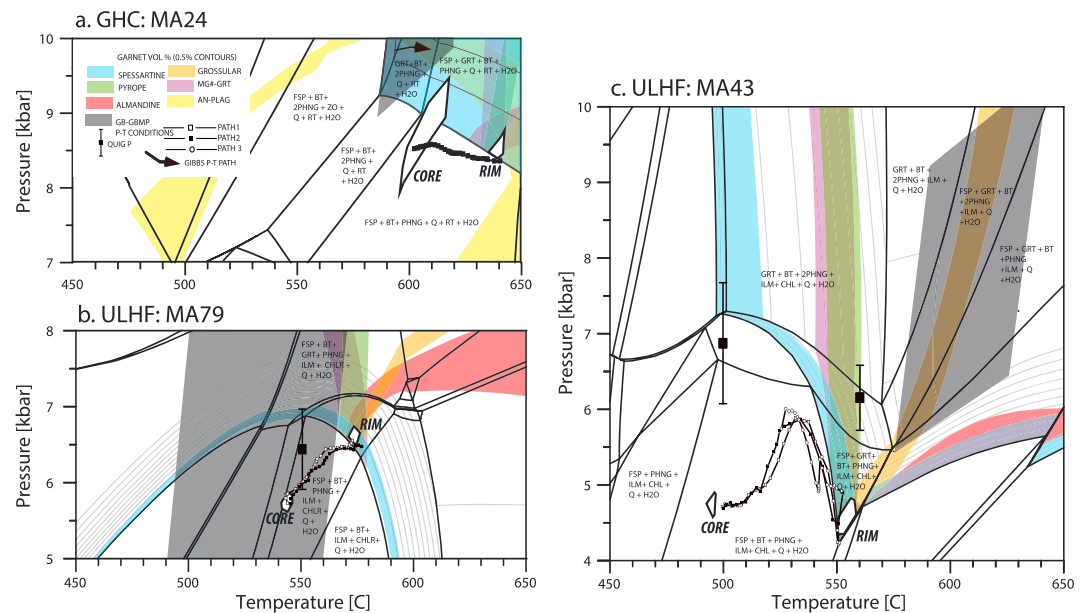
Figure 6. Isochemical phase diagrams for samples (a) MA24, (b) MA79, and (c) MA43 using the rock bulk compositions in Table 3. See Figure 1 for sample locations. Fields of pertinent mineral assemblages are labeled. Overlain on each diagram are lines of garnet volume in 0.5% contours and garnet rim compositions (colored regions). P-T conditions and a Gibbs P-T path (black arrow) are overlain on the figures as reported in Catlos et al. (2001) for these same samples. Only sample MA24 (panel a) has a reported P-T path, whereas only T was estimated for sample MA79 (b, shaded area). (a) The anorthite composition of plagioclase is also overlaid on the diagram for sample MA24. One Theriak-domino P-T path for this sample extends from core to rim and was developed using garnet compositions in Figure 3. (b) QuiG pressures are indicated for quartz inclusions in the core and rim of a garnet in sample MA79. Two Theriak-domino P-T paths extend from core to rim and were developed using garnet compositions in Figure 4. (c) QuiG pressures are indicated for quartz inclusions in the core and rim of a garnet in sample MA43. Three paths were estimated using compositions for sample MA43 using garnet compositions in Figure 4. Abbreviations: GHC = Greater Himalayan Crystallines; ULHF=Upper Lesser Himalaya Formation. Mineral abbreviations after de Capitani and Brown (1987) and de Capitani and Petrakakis (2010), and PHG = muscovite, and 2PHG = potassic- and paragonitic-rich white micas.

typically observed. Thus, minor modifications were made to the bulk composition of these rocks. The changes were done using the Theriak-Domino program in which a back calculation is applied to the rock bulk composition aimed to be the minimum necessary to identify the conditions appropriate for garnet growth. These changes are <0.7% of the results obtained using the XRF or ICP-MS data and did not affect the Na_2O, K_2O, TiO_2, or P_2O_5.

The final, effective bulk composition generated by the Theriak-Domino approach is used to generate the phase diagram for a garnet rim and is a product of the modeling procedure (Tables 3 and 4; e.g., Evans, 2004). The effective bulk composition differs from the XRF or FUS-ICP bulk rock compositions, but the change is minor. Differences between input bulk rock compositions and effective bulk composition average 1.00 ± 0.57 mol% SiO_2, 0.66 ± 0.38 mol% Al_2O_3, 0.71 ± 0.42 mol% Fe_2O_3, 0.07 ± 0.03 mol% MnO, 0.06 ± 006 mol% MgO, and 0.16 ± 0.08 mol% CaO. The species Na_2O, K_2O, TiO_2, or P_2O_5 are unaffected. Despite these small changes, the topology of the phase diagram changes significantly from the initial and rim conditions of garnet growth (Figures 2, 6, and 7). We consider the effective bulk composition as the best representation of local conditions at the garnet rim, whereas the XRF or FUS-ICP bulk composition is the composition accessible for initial garnet growth in a closed system. Overall, the approach has inherent uncertainty that leads to challenges in interpreting the absolute values of the resulting P-T conditions (see discussion in Palin et al., 2016). The approach to the data set prescribes that each high-resolution P-T path reported here is an estimate that approximates the reality of the sample collected. We have confidence in the effective bulk compositions that were applied here (Tables 2–4), as a primary indication of the failure of the models is the lack of intersection of garnet composition isopleths. This can occur and is usually due to significant changes in the rock chemistry during garnet growth, polymetamorphism, or modifications in garnet chemistry due to
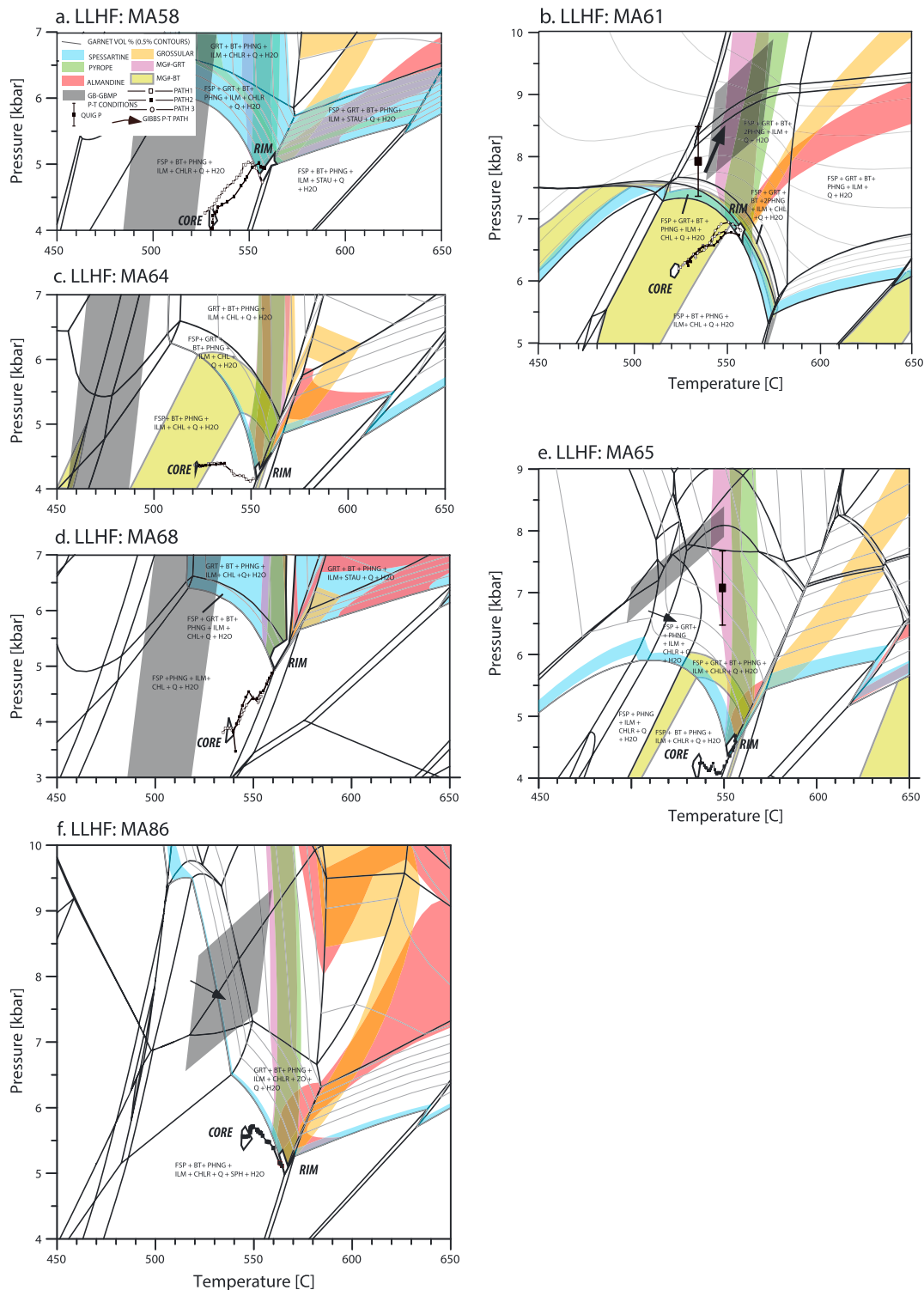
Figure 7. Isochemical phase diagrams for samples (a) MA58, (b) MA61, (c) MA64, (d) MA68, (e) MA65, and (f) MA86 using the rock bulk compositions in Table 4 and garnet compositions in Figures 4 and 5. See Figure 1 for sample locations. Fields of mineral assemblages are labeled. Overlain on each diagram are lines of garnet volume in 0.5% contours and garnet rim compositions (colored regions). The Mg-# for biotite is overlain in the diagram for samples (b) MA61, (c) MA64, and (e) MA65. The Gibbs P-T path and P-T conditions are from Catlos et al. (2001). QuiG pressures are indicated for quartz inclusions in the garnet in samples (b) MA61 and (e) MA65. Abbreviations: ULHF=Upper Lesser Himalaya Formation; LLHF = Lower Lesser Himalaya Formation. Mineral abbreviations after de Capitani and Brown (1987) and de Capitani and Petrakakis (2010).

thermally induced diffusion. Samples that experienced these events cannot be modeled using the approach describe here.

5. Results

5.1. Garnet-Forming Reactions and Approximate Core Conditions

The phase diagrams (Figure 2) suggest that garnet in all samples appeared via a reaction involving the dehydration of chlorite. Each phase diagram shows the mineral assemblage fsp + bt + phng + ilm + chl + q + H_2O at lower P-T conditions, whereas the garnet core appears in the fsp + grt + bt + phng + ilm + chl + q + H_2O stability field, with the exception of GHC sample MA24, which also contains rutile. Overall, the core P-T conditions for each sample lie within a mineral assemblage that is consistent with observations in thin section.

Although we may not have analyzed the true garnet core, the core P-T results we report are our closest approximation and isopleths of garnet growth contours (Figure 2) help evaluate the assumption. All core P-T conditions overlap the 1% volume garnet growth contour, except sample MA24. This garnet has core conditions that plot the furthest from the garnet-in reaction line, within the 3–5 vol.% garnet contours (Figure 2a). The conditions may be the result of using compositions that are midrim as opposed to the real garnet core and/or reaction overstepping (Spear et al., 2014). Results from all LHF samples are near the garnet-in reaction line and are inconsistent with overstepping (Figure 2), especially considering that the analyses used for the calculation are only our closest approximation of the conditions of the true garnet core due to the sectioning of the rock thin section.

GHC sample MA24 records the highest Theriak-Domino core P-T conditions of all rocks analyzed (580 ± 50 °C, 8,650 ± 1,200 bars) and differs from LHF rocks in that its core mineral assemblage contains rutile. The polygon formed by the intersection of garnet isopleths in this sample cover a more extensive P-T range compared to LHF samples that have polygons that cover <400 bars and <8 °C (Figure 2). Although we report uncertainty in P-T conditions using the polygons' range (Table 1), these are underestimates and do not take into account systematic uncertainties associated with the raw data and thermobarometric calculations. Taking these into account would not affect overall trends.

The conditions recorded by garnet cores using the Theriak-Domino approach are consistent with field observations of inverted metamorphism in the footwall of the MCT. For example, sample MA43, collected just beneath the mapped structure and at structurally shallower levels within the LHF, yields a core P-T condition of 490 ± 3 °C and 4,752 ± 250 bars. This is ~60 °C and ~750 bars lower than the structurally lowest sample collected (MA86, ~20 km south; Figure 1 and Table 1). Sample MA86 contains Pliocene monazite grains that are significantly younger than the Eocene to mid-Miocene monazite ages recorded by rocks surrounding sample MA43 (Figure 1c). The discrepancy may reflect a different timing of metamorphism. Lower LHF sample MA65 collected ~7 km NW from sample MA86 contains Miocene age monazite grains, so if sample MA86 experienced an initial phase of Miocene metamorphism, then it is unrecorded by its radiogenic element-bearing minerals. An alternative explanation might lie in control exerted by rock bulk composition (Gaidies et al., 2015). Sample MA43 has the highest amount of MnO of all rocks analyzed (Table 2) and thus potentially initiated garnet growth at lower T.

The conditions recorded by garnet cores using the Theriak-Domino approach also show lateral differences in P-T conditions across the strike of the MCT. For example, sample MA79 yields core conditions that are ~50 °C and 950 bars higher than sample MA43, which is collected ~10 km to the east and at a similar structural location with respect to the mapped MCT (Figure 1). Both rocks have ~0.1 wt% MnO (Table 2), but sample MA79 has higher Fe_2O_3, MgO, and CaO and yields a phase diagram topology similar to that of lower LHF sample MA86 (Table 2 and Figure 2). The MA79 garnet yields core conditions that overlap those recorded by MA86 (Table 1). We have no age constraints specifically for sample MA79, but Eocene to early Miocene monazite ages are found in rocks at similar structural locations (Figure 1c).

Lateral heterogeneity is also seen at structurally lower levels of the LHF. For example, garnets in sample MA61, collected ~3 km directly west of sample MA58 (Figure 1d) record similar T (~530 °C; Table 1), but the MA61 garnet yields a P > 2,000 bars compared to MA58. Sample MA61 has a phase diagram topology similar to samples MA79 and MA86, whereas the phase diagram for sample MA58 more closely resembles LHF samples MA65 and MA64. Sample MA58 also yields similar P-T results as these rocks.

The Theriak-Domino P-T core conditions show no trends with a structural location within the LHF, except a set of samples (MA61, MA64, MA65, and MA68; Figure 1). These rocks record a decrease in P (2,350 bars) southward from sample MA61 to sample MA68 (Table 1) at a T of 530 ± 5 °C. The garnet in southernmost sample MA68 records the lowest core P conditions of all rocks analyzed (3,825 ± 390 bars; Table 1), whereas garnet in MA61 records the highest core P among all MCT footwall samples (6,175 ± 177 bars).

We model the garnet core P-T conditions as reflecting the onset of metamorphism due to movement along and within the MCT shear zone (see also Kohn, 2016). Alternative options exist, such as passive burial, but the structural location of the samples within a major Himalayan fault system strongly suggests that the thermal energy necessary to initiate garnet growth in these rocks was likely facilitated by motion within the fault zone. These samples also have monazite ages that are consistent with the timing of episodes of activity linked to the MCT. Monazite ages are ideal for evaluating the timing of garnet growth, as the mineral appears in these rocks at conditions similar to those coincident with garnet stability (e.g., Catlos et al., 2001; Foster et al., 2000; Mottram et al., 2015), and inclusions in garnet can be armored and shielded from Pb loss (e.g., Montel et al., 2000). Monazite grains from single samples that yield a range of ages are interpreted to reflect multiple episodes of crystallization and dissolution-reprecipitation reactions of preexisting monazite (e.g., Rasmussen & Muhling, 2007). Based on monazite ages, the MCT at this location records deformation that spans the Eocene to Pliocene (Figure 1c; Catlos et al., 2001). We evaluate the timing of core thermobarometric results in the context of P-T paths in the next section.

5.2. Garnet P-T Paths

All P-T paths generated using Theriak Domino approach increase in T, as expected as garnet grows (e.g., Spear, 1993; Figures 6 and 7). The approach will not record garnet growth as T decreases, as retrograde reactions occur. Retrograde reactions are unable to be modeled using the methods described here. The average T path length generated is 29 ± 10°, with the largest T increase recorded by sample MA43 (~52°) and the smallest by Path 2 in garnet MA64 (~14°). Most P-T paths show P fluctuations from ~5 to ~2,000 bars; only garnet in sample MA79 yields a steady P-T increase (Figure 6). The ability to translate minor P changes of 5 bars as tectonically meaningful likely overestimates the ability of Theriak-Domino approach to resolving changes at that scale. However, the larger P drop seen in sample MA43 is likely significant and is considered in the modeling process.

5.2.1. Hanging Wall (GHC) P-T Path

GHC sample MA24 garnet increases in P from core to midrim by ~50 bars, followed by a decrease in P from midrim to rim by ~210 bars (Figure 6a). The baric conditions are recorded over a 40 °C interval and suggest growth at a relatively stable P regime at a depth in the crust that allows <1 km of burial and exhumation during its entire growth history (assuming a geobaric gradient of ~285 bars/km). Monazite Th-Pb ages were not determined for MA24. Surrounding assemblages contain monazite inclusions in garnet that are from Eocene (37.5 ± 0.3 Ma), Oligocene (30.4 ± 0.5 Ma, 29.2 ± 0.5 Ma, and 26.1 ± 9.6 Ma), early Miocene (18.5 ± 0.5 Ma) to late Miocene (6.3 ± 0.3 Ma; Figure 1c; Catlos et al., 2001). The range of ages from inclusions in garnet from nearby samples suggests that the GHCs record multiple episodes of metamorphism over a considerable time interval.

5.2.2. Footwall (Upper LHF = MCT Shear Zone) P-T Paths

Samples MA79 and MA43 are the only upper LHF samples analyzed for P-T path calculations (Figures 1d, 6b, and 6c). Three P-T paths along a garnet in sample MA43 are hairpin (P increase followed a P decrease over a short T interval), whereas two paths along a garnet in sample MA79 show an overall P-T increase. The peak P-T conditions recorded by sample MA43 at ~535 °C and ~5,900 bars are similar to the garnet core P-T conditions for sample MA79 (544 ± 6 °C, 5,700 ± 280 bars; Table 1). Sample MA79 increases in P by ~900 bars over the 540–580 °C interval, yet sample MA43 decreases in P by ~2,000 bars over a similar T interval (530–550 °C).

The exhumation portion of the P-T path recorded by sample MA43 requires an additional heat source to provide ~20° recorded by its garnet from midrim to rim. Garnet will not grow during a T decrease because retrograde reactions facilitate its dissolution. Sharp decreases in P follow the exhumation portion of the P-T path in sample MA43. The final part of Path 1 increases by ~155 bars and Path 2 by ~415 bars at the rim, whereas the exhumation portion of Path 3 increases by ~425 bars at the midrim, followed by the decreasing P trend.

5.2.3. Footwall (Lower LHF) P-T Paths

All samples from the LHF show changes in P as T increases. We report three paths for sample MA58 and two paths each for samples MA61 and MA64. All indicate that garnet formed over similar T interval, from 520 °C to 560 °C but at different P. Samples MA61 and MA58 may not record more of the exhumation portion of the hairpin path compared to sample MA64 because garnet did not grow as T decreased.

Path 1 from core to rim across garnet in sample MA64 increases in P by 40 bars then decreases in P by ~210 bars. However, Path 2 only yields the 40-bar P increase (Figure 7c). A comparison of garnet zoning profiles across the MA64 garnet shows that the compositions used for Path 2 are likely incomplete, as the lowest spessartine and grossular and highest almandine and pyrope values are recorded by the portion of the garnet that yields Path 1 (Figures 5a–5d). The outer rim of the part of the garnet used to generate Path 2 is likely missing, and thus, it does not record the compositions that produced the P decrease.

Sample MA65 records a W-shaped P-T path, whereas sample MA68 is N-shaped (Figures 7d and 7e). The P fluctuations that control these shapes are small (<50 bars) and may be related to minor changes in composition at specific portions of the garnet. However, a range of monazite ages is reported from the samples, with tectonic activity occurring during the early Eocene to Pliocene. Sample MA65, which records the most complex P-T path, has matrix Th-Pb monazite ages that range from 20.4 ± 1.0 to 9.5 ± 0.4 Ma (Catlos et al., 2001). A range of monazite ages would be expected for samples that experienced P-T path fluctuations. In this case, dissolution-reprecipitation reactions could occur as conditions change and monazite is more susceptible to resetting during subsequent metamorphic events compared to other accessory minerals like zircon (Catlos, 2013).

6. Discussion

6.1. Comparison of P-T Approaches

Temperatures estimated using GB thermometry overlap those for all or part of the Theriak-Domino P-T paths for GHC sample MA24, upper LHF sample MA79, and lower LHF samples MA61, MA65, and MA86 (Figures 6 and 7). However, the GB temperatures are ~70° to 120° higher than those estimated for the rim P-T conditions for upper LHF sample MA43 (Figure 6c). Lower LHF samples record lower temperatures compared to GB thermometry, but still within the uncertainty of the mineral equilibria approach (MA58, by ~7° to 100°, MA64, by ~40° to 120°, and MA68 by ~5° to 100°; Figures 6 and 7).

All samples show higher GPBM pressure conditions compared to the Theriak-Domino approach (Table 1). The smallest difference in P is observed in GHC sample MA24, which has lower Theriak-Domino pressures by 70 to 1,370 bars. The largest P difference is seen in sample MA43, which has lower Theriak-Domino pressures by 3,200 to 5,200 bars compared to those estimated using GPBM.

Gibbs P-T paths overlap in temperature with those estimated using Theriak-Domino for samples MA24 and MA61 but yield lower temperatures in samples MA65 and MA86 (Figures 6 and 7). Although Gibbs P-T paths show higher P conditions compared to those generated using Theriak-Domino, the Gibbs P-T paths follow the same general trends of all or portions of paths as those indicated by Theriak-Domino.

Upper LHF samples MA43 and MA79 and lower LHF samples MA61 and MA65 were subjected to QuiG barometry. Pressures estimated using QuiG are overall higher than those suggested by the Theriak-Domino approach, except the core inclusion in sample MA79, which overlaps conditions along its P-T path (Figure 6b). The most significant difference in QuiG P compared to the Theriak-Domino rim conditions is seen in sample MA65, which differs by 2,000 to 3,760 bars, depending on uncertainty (Figure 7). Upper LHF sample MA79 is the only rock in which overlapping conditions result using the modeling, QuiG barometry, and GB thermometry (Figure 6). QuiG P are more similar to conditions estimated using mineral equilibria, as opposed to Theriak-Domino, except for sample MA79 (Table 1).

Differences between P-T conditions for the same data set estimated using different conventional calibrations are commonly reported (e.g., Holdaway, 2004; Spear, 1993). More recently, comparisons have been made between conditions obtained using QuiG and conventional barometry (Plumhoff & Spear, 2016; Spear et al., 2014; Wolfe & Spear, 2015a, 2015ab, 2016). The results we observed with higher QuiG pressures compared to the Theriak-Domino estimates are also discussed in these studies (see review in Spear et al., 2014). Garnet isopleth boundaries estimated using Theriak-Domino are sensitive to rock bulk composition, and their

steep slopes lead to more challenging estimates for P (Mattinson et al., 2014; Palin et al., 2016). The An content of plagioclase content controls the baric conditions seen with the mineral equilibria approach (e.g., Hoisch, 1990; Spear, 1993), whereas QuiG barometry is independent of garnet compositions. The application of Theriak-Domino P-T path modeling and conventional thermobarometric approaches requires the use of mineral chemistry.

At this stage, a resolution of which approach should be used to obtain the most accurate pressures is unclear. Our evaluation is that no method is more accurate than others, but instead, each is limited by our understanding of thermodynamic models of mineral reactions in natural systems. Results reported here should not be viewed a providing a "true" or "correct" version of the conditions the rocks truly experienced. Fundamentally, we apply our best understanding of thermodynamics to model a natural system that has a series of embedded uncertainties: from bulk rock, electron microprobe, and structural setting to modeling (petrology and thermomechanical) constraints (see discussion in Palin et al., 2016). Ultimately, the high-resolution Theriak-Domino P-T paths generated here are an approximation of how a garnet with a specific type of compositional zoning would behave in a system of a specified bulk composition that evolves during its growth. Uncertainties lie in the input data (bulk rock and mineral compositions) and our understanding of the thermodynamics of mineral reactions (Palin et al., 2016). In most cases, the paths themselves reproduce what would be expected for garnet zoning in the samples at a level of <0.01-mole fraction (Figures 3–5). Further confidence is supported by matrix mineral P-T conditions in some samples that overlap or lie near garnet rim conditions (MA24, Figure 6, and MA58, MA64, MA61, and MA65, Figure 7). The consistency of paths along multiple transects across garnet in the same sample and from rocks collected in close proximity also indicates that they are useful for understanding how the region evolved during metamorphism.

Ideally, all of the thermodynamic approaches should result in the same P-T conditions (which occurs with sample MA79), but differences may be the result of recording different events along a sample's P-T path and/or limitations of thermodynamic models of mineral reactions in natural systems. The modeled paths reported here are our best estimates of the nature of rock motion across the MCT shear zone. The path shape should be considered more robust than the specific conditions, although the conditions match rock mineral assemblages and reproduce garnet zoning. We use the Theriak-Domino conditions primarily to constrain a thermomechanical model of Himalayan collision in the following section.

6.2. Tectonic Modeling of P-T Paths
6.2.1. Original Imbrication Model: P-T Path Predictions

The shapes of the Theriak-Domino modeled P-T paths indicate the potential for imbrication in the MCT footwall (Kohn, 2008; Kohn et al., 2001). Thus, we aim to evaluate their predictions in the context of models that anticipate this behavior in the MCT shear zone (Caddick et al., 2007; Catlos et al., 2001; Groppo et al., 2009; Harrison et al., 1998; Herman et al., 2010; Mosca et al., 2012). Ultimately, we chose the thermokinetic model of Harrison et al. (1998) as it makes predictions regarding the P-T evolution of rocks across the MCT from 25 to 2 Ma. This particular model was used to gauge if its assumptions and approach produce P-T paths that are similar in shape and condition as those generated using the Theriak-Domino approach. Other, more recently developed models could have been used (see Imayama et al., 2010; Larson et al., 2013, or Rolfo et al., 2014, for similar approaches); however, the Harrison et al. (1998) model was developed using the rocks analyzed in this study and consists of a quantitative framework that predicts P-T path trajectories for multiple samples.

In the Harrison et al. (1998) model, thermobarometric histories are calculated using a two-dimensional finite difference solution to the diffusion-advection equation (summarized in Figure 8). The location of thrust faults (Main Himalayan Thrust [MHT], MCT, and Main Boundary Thrust [MBT]) in the model is based on seismic and structural interpretations (see discussion in Harrison et al., 1998). Parameters appropriate to crustal rocks in terms of thermal conductivity [2.5 W/(m^{-K})], diffusivity (8×10^{-7} m^2/s), heat capacity (1 kJ/kg^{-K}), latent heat of fusion (400 kJ/kg), basal and initial surface flux (30 mW/m^2, 70 mW/m^2), and radioactivity length scale (15 km) are incorporated. The displacement velocity is partitioned equally between the hanging wall and footwall (20 mm/yr speed rate); no topography (denudation = uplift) and an initial uniform geotherm are considered. The MCT slip rate is the sum of hanging wall and footwall speeds along the fault. When the model is activated, rocks move at similar speeds (20 mm/yr) in the direction specified by the fault. The model aims primarily to describe the generation of the High Himalayan leucogranites and North Himalayan granites, although MCT footwall imbrication is also incorporated. Departure from these, including ones proposed in
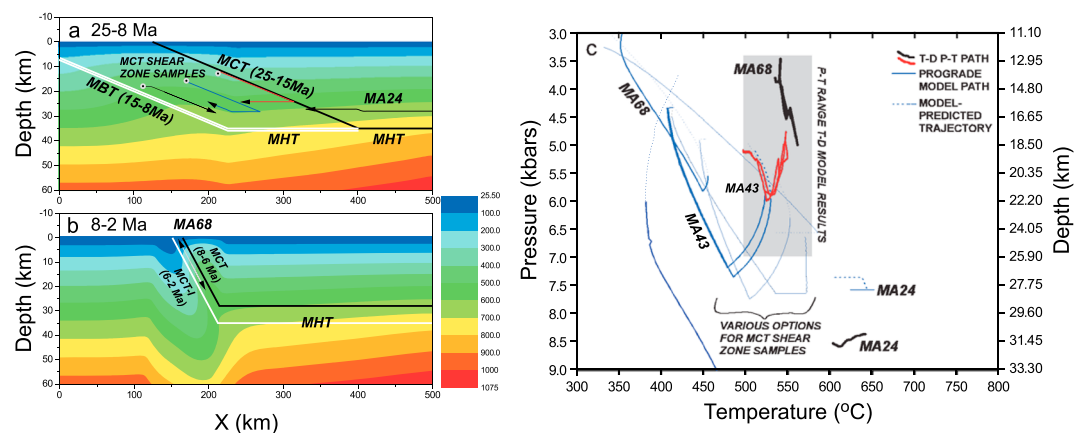
Figure 8. (a) Thermal-kinematic model cross section showing the MCT (dark line) and MBT (white line) from 25 to 8 Ma. The MCT and MBT sole into the MHT at depth. Isothermal sections in degree increments are indicated by the color scale bar. Panel (a) is meant to show the thermal situation at 8 Ma after rocks have moved along their trajectories. These are represented by arrows with dots at the initial and heads at the final positions. Sample MA24 is labeled, and three different possible tracks for MCT shear zone rocks are shown. These include burial, isobaric cooling, a, or combinations. (b) The model cross section from 8 to 2 Ma. In this case, the MCT and MCT-I sole into the MHT at depth. This panel is meant to represent the thermal situation at 2 Ma, and the development of MCT shear zone inverted metamorphism. Sample trajectory for MA68 is indicated as an example. The sample experienced burial followed by exhumation, thus the two arrowheads. (c) Diagram showing predicted P-T paths by the Harrison et al. (1998) thermal model for hanging wall (MA24), various MCT shear zone, and footwall samples, including MA43 and MA68. Gray box indicates the P-T region covered by the Theriak-Domino conditions (see Table 1). Dashed lines are the retrograde portion of the paths and would not be recorded by garnet. Note the discrepancy between the predicted and the Theriak-Domino generated P-T paths and conditions.

the modification discussed here, does not significantly affect the conclusions regarding the production of melt in the zone.

Using this model, we generated P-T paths for equivalent structural positions as those collected in this study and compared them to the shapes and conditions produced using the Theriak-Domino approach (Figure 8). In this scenario, samples move over a thrust flat-ramp geometry at different times along the MCT, MHT, or MBT (Figure 8a). Slip is accommodated along the MHT-MCT ramp between 25 and 15 Ma and along the MBT-MHT ramp from 15 to 8 Ma. At 8 to 2 Ma, fault ramps within the LHF become active, labeled as the MCT from 8 to 6 Ma, and MCT-I from 6 to 2 Ma (Figure 8b). These time frames were dictated based on monazite and $^{40}Ar/^{39}Ar$ ages from rocks collected within the MCT shear zone (see Harrison et al., 1998). The dip angle of both faults is higher (30°) from 8 to 2 Ma compared to the angle of the MCT between 25 and 18 Ma (7°). The flat ramp of the MCT-I (labeled as the MHT in Figure 8b) is below that of the MCT.

The thermal-kinematic model predicts peak P-T conditions that match some of the results from samples from the MCT footwall using GB thermometry and GPBM and QuiG barometry. The model is based on conventional thermobarometric data and thus should be expected to be consistent with those data. For example, sample MA64 records a peak GB T of 475 ± 35 °C, consistent with the model's prediction of a cooler footwall. The path generated for sample MA68 reaches a maximum T of ~450 °C, within reasonable uncertainty with what is predicted by GB thermometry (513 ± 38 °C). Although some samples should record very high P at low T (Figure 8c), QuiG P for MCT shear zone (upper LHF) samples ranges from 6.15 ± 0.43 (MA43) to 7.92 ± 0.56 kbar (MA65), consistent with the majority of model outcomes for the MCT footwall.

However, using the time frames and parameters in Harrison et al. (1998) produces P-T paths incompatible with estimated Theriak-Domino P-T paths and conditions (Figure 8c). The main discrepancies involve T: the model predicts a hotter hanging wall and a colder footwall that what is observed with the Theriak-Domino P-T paths. For example, the rim thermal conditions for GHC sample MA24 at ~30 km (~8.6 kbar) would be in the range of 600–640 °C (Table 1). At this P, the model predicts that the sample would have experienced $T > 700$ °C (Figures 8a and 8c). Upper LHF samples only reach the 550–570 °C values suggested using Theriak-Domino at levels 5–10 km deeper (i.e., more than ~2 kbars) than the Theriak-Domino P recorded by the analyzed samples.
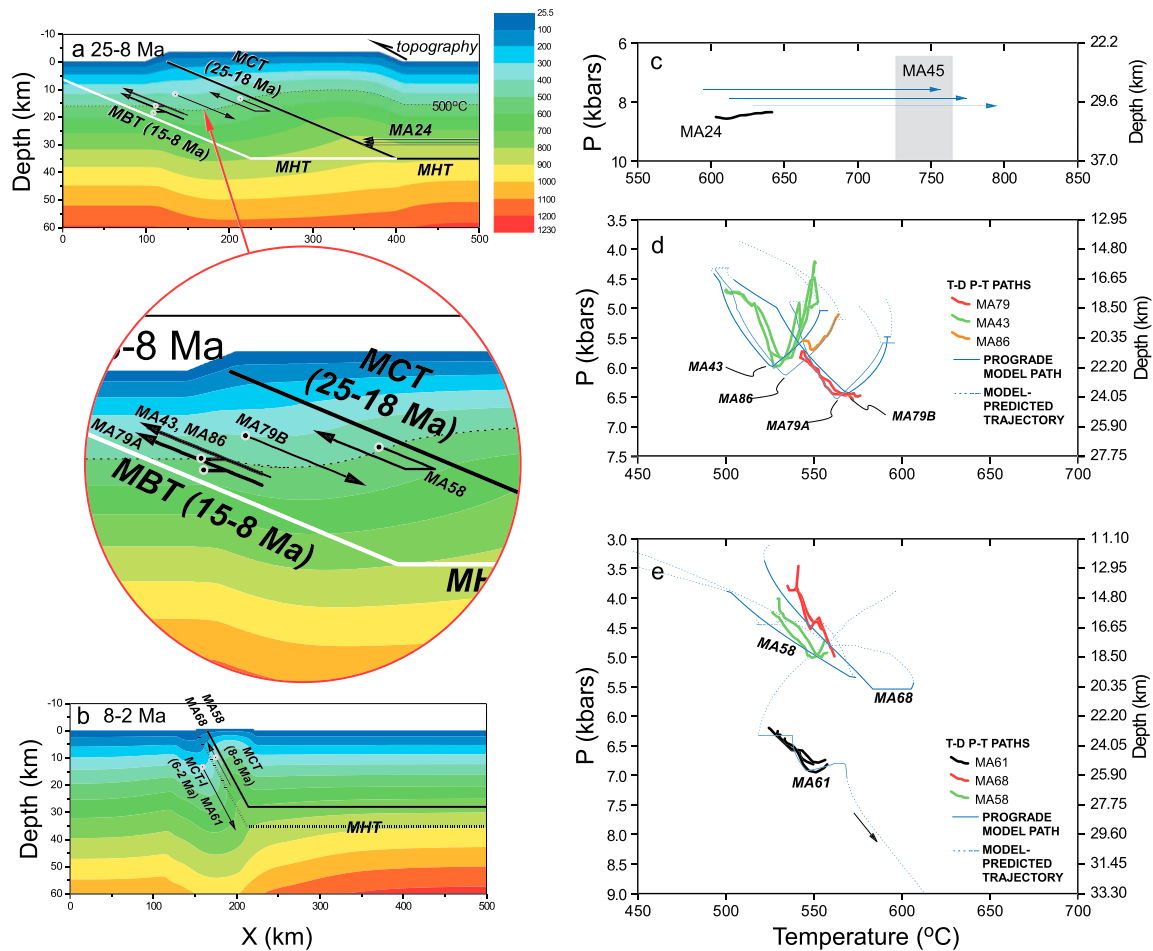
Figure 9. (a) Thermal-kinematic model cross section showing the MCT (dark line) and MBT (white line) from 25 to 8 Ma. The MCT and MBT sole into the MHT at depth. Isothermal sections in degree increments are indicated by the color scale bar. Panel (a) is meant to show the thermal situation at 18 Ma after MCT slip. These trajectories are represented by arrows with dots at the initial and heads at the final position. Sample MA24 is labeled, and three different possible tracks for this rock are shown. The inset shows the locations of samples MA58, MA43, MA86, and two options for the position of sample MA79 (represented by samples MA79A and MA79B). Samples MA43, MA86, and MA79B move toward the right of the model, down, and then up. The MCT is active from 25 to 18 Ma, whereas slip transfers to the MBT from 15 to 8 Ma. (b) The model cross section of the reactivation of the MCT shear zone from 8 to 2 Ma. In this case, the MCT and MCT-I sole into the MHT at depth. This panel is meant to represent the thermal situation at 6 Ma right before the development of MCT shear zone inverted metamorphism. Sample trajectories are shown for samples MA58, MA68, and MA61. (c) P-T paths for Greater Himalayan Crystallines sample MA24 and three options for possible matching trajectories. We also indicate P-T conditions for Greater Himalayan Crystallines sample MA45 (Table 1). (d) P-T paths for samples MA79, MA43, and MA86 generated using the Theriak-Domino model approach and those predicted by modifications to the Harrison et al. (1998) thermal model. (e) P-T paths are plotted for samples MA61, MA68, and MA58. In both panels (d) and (e), dashed lines show the retrograde portion of the paths (decreasing T) or continued movement through the model (increasing T).

6.2.2. Modified Imbrication Model: P-T Path Predictions

The Harrison et al. (1998) model fundamentally measures heat flow at particular locations due to varying conditions; thus, to fit the P-T paths, specific parameters required modification. To obtain a better fit of the Harrison et al. (1998) model suggested P-T paths with Theriak-Domino P-T paths and conditions, we incorporated four changes, focusing primarily on the 25–15-Ma time frame (Figure 9a). Instead of maintaining at 10-km/Ma MCT footwall speed rate, we reduced this to 5 km/Ma from 25 to 18 Ma. The footwall speed rate is the rate that the sample travels along the MCT within the Lesser Himalayan Formations. The hanging wall speed rate is maintained at 10 km/Ma, and topography progressively accumulates until a maximum height of 3.5 km. The increase in topography is required to accommodate the pressure changes recorded by the garnets while matching their thermal histories. Without this topographic change, the model cannot fit the Theriak-Domino P-T paths reported here. Once the topography is achieved at 18 Ma, a period of nonslip is introduced between 18 and 15 Ma. In our model, this represents the cessation of the MCT and onset of the MBT. During this nonslip period, the topography is reduced at a

AGU
100
ADVANCING EARTH
AND SPACE SCIENCE

Tectonics

10.1029/2018TC005144

rate of 1.5 km/Ma. Again, this is done to match the Theriak-Domino P-T paths. After these changes are incorporated (Figure 9a), the model returns to activity within the MCT shear zone with the activation of the MCT from 8 to 6 Ma and MCT-I from 6 to 2 Ma (Figure 9b).

In the modified scenario, part of the P-T paths recorded by the footwall garnets results from thermal advection combined with alteration of topography. The pressure that garnet records can be due to burial or alteration (emplacement or erosion) of a topographic overburden. The emplacement of overburden or burial increases pressure, whereas erosion decreases pressure. Because garnets in our field area grow during increases in temperature (see % volume growth lines in Figure 2), advection can work to cool a sample and halt garnet growth. All samples are displaced by motion along the MCT, MCT-I, and MBT during particular periods specified in the model, but garnets here can only record P-T paths during an increase in temperature.

The Theriak-Domino P-T paths cannot be reproduced by the Harrison et al. (1998) model if only a single phase of Miocene MCT motion is imposed. The P-T paths themselves require footwall imbrication and the outlined modifications. These changes result in a better fit between the model prediction and estimated conditions for six P-T paths (MA43, MA58, MA61, MA68, MA79, and MA86; Figure 9). The exceptions are samples MA24, MA64, and MA65 (Figure 9). The isobaric trajectories with increasing T seen in MCT footwall samples MA64 and MA65 are unable to be accommodated by the Harrison et al. (1998) model and our proposed modifications. These paths suggest motion along local flats within the LHF and are trajectories unable to be modeled by this larger-scale global approach. Their paths may be the result of deformation and heating of local structures within the shear zone. We indicate the possible presence of these in Figure 1d, where some local structures are visible in the field south of samples MA43 and MA81.

We estimated three possible depths (26.6, 27.5, and 28.5 km) for the isobaric trajectory of GHC sample MA24 as it moved along the MHT flat. Motion along a décollement or other shallowly dipping structure within the MCT hanging wall allows P to remain constant. For each scenario, the sample's maximum T (640 ± 7 °C, Theriak-Domino rim, or 600 ± 18 °C, GB thermometry; Table 1) are 100 to 200° lower compared to the modeled hanging wall peak T at increasing depths (756 °C, 777 °C, and 797 °C, respectively). We speculate that at a rate of 10 km/Ma, sample MA24 must have been displaced several tens of kilometers over the flat ramp during the MCT slip. Thus, the conditions recorded by sample MA24 values could be the result of growth over cooler crust farther away from the currently placed MCT.

All other rocks (*n* = 6) show a reasonable fit with the results, including samples MA43 and MA79, which are collected at similar structural levels near the MCT but show different paths (hairpin and increasing P-T, respectively; Figure 9d). The modeled fit indicates that their differences in condition and shape are not an outcome of locally varying conditions. The path recorded by sample MA79 could be recorded by a sample near MA43 (represented by MA79A in Figures 9a and 9d) or one closer to the GHC (MA79B in Figures 9a and 9d). In the evaluation of model P-T paths for fit with the Theriak-Domino results, we aimed to place the samples as close as possible to what is indicated by their structural location but also explored where rocks yield particular paths. In both cases for sample MA79 (identified as MA79A and MA79B), garnet growth initiates near the peak P-T conditions recorded by sample MA43. The exhumation (retrograde) portion of their history is not recorded. The model also predicts that garnet growth in sample MA86 (Figure 9d) would have initiated at peak conditions recorded by MA43, but followed a P decrease, instead of the burial trend as seen in sample MA79.

The hairpin-shaped P-T path as seen in sample MA43 requires a pause in footwall motion combined with rapid denudation of the surface to account for the significant drop (i.e., ~1.5 kbars or ~5 km) in P and monotonic increment of T increase recorded by the garnet rim. Any decrease in P of that magnitude in the presence of advection should lower sample T, which is not observed. Thus, we suggest that the P decrease is due to rapid denudation, as opposed to fault slip. Denudation allows a rebound of T at depth as a result of the pause in subduction and heat supply from the hanging wall, asthenosphere, and input from radioactivity to permeate throughout the footwall. With these constraints, erosion will work to reduce P without significantly affecting sample T. Overall, data from sample MA43 appear to indicate substantial erosion (~3 km) during the nonslip pause. The timing of this break in activity overlaps the deposition of the Siwalik sediments at the foreland of the Himalayas (e.g., Bernet et al., 2006; Brewer et al., 2003; Ruhl & Hodges, 2005; Szulc et al., 2006; White et al., 2002).

In principle, the growth of garnets proceeds during periods of monotonically increases in increments of sample T. The P-T diagram in Figure 9 has solid lines that represent that portion of the history and dashed lines that correspond with periods when sample T decreases. In some cases (MA58, MA68, MA61, and MA79B), the model predicts P-T conditions along the solid line that exceeds what is estimated by the garnet records. The overestimate could be the result of garnet growth starting later or ending before reaching the optimum favorable thermal conditions. The uncertainty in the thermodynamic modeling also likely overlaps the model-predicted peak conditions. Some samples show the beginning of the hairpin decline in P (MA61 and MA58; Figure 9d) but stopped possibly due to lack of Mn supply or a sharp decrease in T.

From 8 to 2 Ma, the model continues the imbrication process with the activation of the MCT-I (Figure 9b). In this scenario, all samples returned to the surface, except MA61, which is buried and records the highest depths of all footwall samples (~24 km). Although we can fit the path of sample MA61, the exhumation of this sample requires very high rates due to its peak P. The P constraint suggested by Theriak-Domino is lower than what is suggested for a majority of samples using conventional approaches and QuiG barometry (Table 1). To match the model P-T results with the Theriak-Domino record for this garnet, the ideal location of the sample is inside the footwall of the MCT at 8 Ma. Once the zone experiences reactivation, MA61 is buried to depths >24 km at 2 Ma. Thus, to move this sample to the surface would require exhumation rates of ~12 mm/yr. Recent thermochronology of detrital minerals in foreland basin sediments suggests that the Himalayas have sustained extremely rapid exhumation rates (>5 mm/yr) since 5 Ma (Lang et al., 2016). The current Himalayan convergence rate is 17.8 ± 0.5 mm/yr in central and eastern Nepal and 20.5 ± 1 mm/yr in western Nepal (Ader et al., 2012). A combination of erosion and continued activity within the MCT shear zone locally may have operated to drive exhumation of this rock. In any case, the model and garnet P-T conditions open the possibility of very high exhumation rates within the MCT shear zone since the Pliocene.

6.3. Alternative Interpretations and Considerations

We use values here for activity along the MCT and MCT-I based on monazite and [40]Ar/[39]Ar muscovite ages from this particular transect (Bollinger et al., 2004; Catlos et al., 2001), which are consistent with what has been reported elsewhere, at least in its Miocene onset (see review in Yin, 2006). We recognize that most samples across the Marsyangdi transect yield monazite ages inconsistent with a single population (Figure 1c). In any case, the Harrison et al. (1998) model and its modification require data regarding the duration, location, and rate of slip along Himalayan structures. Ages of monazite inclusions in garnet and reported [40]Ar/[39]Ar muscovite ages are used only as a guide to inform the model when the MCT and MCT-I were active. The timing of MBT activity is suggested to be >11 Ma (see review in Yin, 2006), but this is not well constrained, and other imbricate structures exist south of the MCT and north of MBT that may also be potential candidates to accommodate a transfer of activity (e.g., Carosi et al., 2018; DeCelles et al., 2001; Hauck et al., 1998; Robinson & Martin, 2014). We choose the MBT as it is a significant thrust system that appears to have operated at the time indicated. Other alternative imbricate structures could have also been active alternatively or synchronously and would not affect the interpretations outlined here.

Sample MA24 was the only GHC sample used to produce a P-T path because all other hanging wall samples were significantly affected by diffusion. Diffusional modification of garnet is predicted by the thermokinematic modeling. The conventional T data and QuiG P for estimated for GHC sample MA45 (Table 1) more closely match the peak conditions suggested by the trajectories for hanging wall rocks. The South Tibetan Detachment System or other internal structures recently proposed to be present in the GHC (e.g., Ambrose et al., 2015; Hodges et al., 1998; Iaccarino et al., 2017; Imayama et al., 2012; Walters & Kohn, 2017) would only disturb the thermal structure of the hanging wall and have no significant influence on the P-T paths taken by the footwall samples. These structures, if present along this transect, do not influence the P-T conditions of GHC sample MA24, which remains at isothermal during its growth period.

Although we make comments regarding the implications of the results to the overall tectonic evolution of the Himalayas, the lateral heterogeneity of the P-T conditions across the strike of the MCT in our samples suggests that a degree of caution should be undertaken to generalize the results of the findings (see also Landry et al., 2016). Others have suggested MCT activity at a time in the range of our proposed tectonic pause (e.g., Kohn et al., 2004, 2005; Larson et al., 2017; Tobgay et al., 2012), whereas in some locations evidence for post-early Miocene monazite crystallization within the MCT inverted metamorphic sequence is missing

(i.e., Arunachal Pradesh, NE India; Clarke et al., 2016). Some locations record Oligocene tectonic activity along the MCT, ~10 m.y. earlier than in central Nepal (e.g., Arun Valley, eastern Nepal; Groppo et al., 2010). We are constrained to data and insight from the samples we analyzed along this specific transect. If similar results are present across the entire range is an open question and one to be resolved with future modeling and analysis. Overall, however, a model that suggests a single episode of slip along the MCT would not reproduce the P-T paths generated here.

7. Conclusions

We report high-resolution model P-T paths using the Theriak-Domino approach for nine garnet-bearing rocks collected across the Himalayan MCT along the Marsyangdi River in central Nepal. QuiG pressures were estimated for six of the samples, and some have previous conditions and paths estimated using mineral equilibria and Gibbs P-T path modeling. Some samples have previously reported Th-Pb monazite ages that suggest multiple episodes of deformation within its footwall (Catlos et al., 2001).

Isochemical phase diagrams generated using the bulk rock compositions for the rocks suggest that garnet in all samples appeared via a reaction involving the dehydration of chlorite. GHC sample MA24 records the highest Theriak-Domino core P-T conditions of all rocks analyzed (580 ± 50 °C, 8,650 ± 1,200 bars). Core P-T conditions from upper and lower LHF garnets range in P from 3,825 ± 390 bars to 6,175 ± 177 bars over a narrow T interval from 490 ± 3 °C to 547 ± 5 °C. Using modeled garnet zoning, P-T paths from the GHC sample suggest garnet growth at a relatively stable P regime at a depth in the crust that allows <1 km of burial and exhumation during its entire growth history. However, most LHF garnets show fluctuations in P from ~40 to ~2,000 bars.

Modeled and mineral equilibria rim P-T conditions and paths, and baric conditions estimated using QuiG barometry, do not yield similar results, except one upper LHF sample (MA79; Figure 6b). The discrepancy reflects differences in fundamental, independent assumptions for the multiple thermodynamic approaches applied here and suggests that the high-resolution P-T paths generated using the Theriak-Domino approach are estimates representing a specific bulk rock and garnet composition that approximates samples collected in the field. Overall, however, the modeled P-T paths reproduce what would be expected for garnet zoning in the samples at a level of <0.01-mole fraction in most cases (Figures 3–5). The consistency of paths along multiple garnet transects from the same rock lends confidence that they are useful for understanding how the mineral grew during rock metamorphism.

The paths were input into the thermokinematic model of Harrison et al. (1998), and forward modeling supports the hypothesis that the inverted metamorphism observed in the footwall of the MCT developed via imbrication and the displacement of distinct rock packages. We propose some modifications of this model to fit the P-T paths, including reducing the MCT speed rate from 5 km/Ma between 25 and 18 Ma and maintaining the speed of the hanging wall at 10 km/Ma while a progressive topography builds to 3.5 km. A pause in slip is introduced for the MCT between 18 and 15 Ma, which, in our model, represents the initiation and transfer of activity to the MBT. During this time, denudation of the buildup topography is active at a rate of 1.5 km/Ma. The majority of the Theriak-Domino P-T paths fits the modified Harrison et al. (1998) modeled P-T paths and thus implies that the MCT may have experienced a period of quiescence during the onset of the MBT. Activation of thrusts within the MCT footwall from 8 to 2 Ma suggests a high rate of exhumation (>12 mm/yr) since the Pliocene.

The approach to generating high-resolution P-T paths we describe here is applied using easily obtained information (major element bulk rock and high-quality mineral compositions). Although the input data used here are from 2001, our ability to interpret their meaning has improved. Others may have similar data on hand that can be processed in a similar fashion to increase understanding of the dynamics of field areas beyond the Himalayas. We caution that garnets with complex zoning profiles, those with drastic changes in composition over short distances, those modified by diffusion, or rocks that experienced major changes in bulk composition over their growth history are not useful candidates. However, even these types of samples may provide clues by exploring the reason for their failure. Ideal samples are those with garnets that preserve prograde, gradational core-to-rim zoning profiles, and these have the potential to transform our understanding of the dynamics of field areas that contain them.

References

Ader, T., Avouac, J.-P., Liu-Zeng, J., Lyon-Caen, H., Bollinger, L., Galetzka, J., et al. (2012). Convergence rate across the Nepal Himalaya and interseismic coupling on the Main Himalayan Thrust: Implications for seismic hazard. *Journal of Geophysical Research*, *117*, B04403. https://doi.org/10.1029/2011JB009071

Ambrose, T. K., Larson, K. P., Guilmette, C., Cottle, J. M., Buckingham, H., & Rai, S. (2015). Lateral extrusion, underplating, and out-of-sequence thrusting within the Himalayan metamorphic core, Kanchenjunga, Nepal. *Lihosphere*, *7*(4), 441–464. https://doi.org/10.1130/L437.1

Anczkiewicz, R., Chakraborty, S., Dasgupta, S., Mukhopadhyay, D., & Koltonik, K. (2014). Timing, duration and inversion of prograde Barrovian metamorphism constrained by high resolution Lu-Hf garnet dating: A case study from the Sikkim Himalaya, NE India. *Earth and Planetary Science Letters*, *407*, 70–81. https://doi.org/10.1016/j.epsl.2014.09.035

Arita, K. (1983). Origin of the inverted metamorphism of the Lower Himalaya, central Nepal. *Tectonophysics*, *95*(1-2), 43–60. https://doi.org/10.1016/0040-1951(83)90258-5

Ashley, K. T., Caddick, M. J., Steele-MacInnis, M. J., Bodnar, R. J., & Dragovic, B. (2014). Geothermobarometric history of subduction recorded by quartz inclusions in garnet. *Geochemistry, Geophysics, Geosystems*, *15*, 350–360. https://doi.org/10.1002/2013GC005106

Ashley, K. T., Darling, R. S., Bodnar, R. J., & Law, R. D. (2015). Significance of "stretched" mineral inclusions for reconstructing P-T exhumation history. *Contributions to Mineralogy and Petrology*, *169*, 1–9.

Ashley, K. T., Steele-MacInnis, M., Bodnar, R. J., & Darling, R. S. (2016). Quartz-in-garnet inclusion barometry under fire: Reducing uncertainty from model estimates. *Geology*, *44*(9), 699–702. https://doi.org/10.1130/G38211.1

Ashley, K. T., Steele-MacInnis, M., & Caddick, M. J. (2014). QuIB Calc: A MATLAB (R) script for geobarometry based on Raman spectroscopy and elastic modeling of quartz inclusions in garnet. *Computers & Geosciences*, *66*, 155–157. https://doi.org/10.1016/j.cageo.2014.01.005

Baldwin, J. A., Powell, R., Brown, M., Moraes, R., & Fuck, R. A. (2005). Modelling of mineral equilibria in ultrahigh-temperature metamorphic rocks from the Anápolis-Itauçu Complex, central Brazil. *Journal of Metamorphic Geology*, *23*(7), 511–531. https://doi.org/10.1111/j.1525-1314.2005.00591.x

Beaumont, C., Jamieson, R. A., Nguyen, M. H., & Lee, B. (2001). Himalayan tectonics explained by extrusion of a low-viscosity crustal channel coupled to focused surface denudation. *Nature*, *414*(6865), 738–742. https://doi.org/10.1038/414738a

Berman, R. G. (1990). Mixing properties of Ca-Mg-Fe-Mn garnets. *American Mineralogist*, *75*, 328–344.

Bernet, M., van der Beek, P., Pick, P. R., Huyghe, P., Mugnier, J.-L., Labrin, E., & Szulc, A. (2006). Miocene to recent exhumation of the central Himalaya determined from combined detrital zircon fission-track and U/Pb analysis of Siwalik sediments, western Nepal. *Basin Research*, *18*(4), 393–412. https://doi.org/10.1111/j.1365-2117.2006.00303.x

Bollinger, L., Avouac, J. P., Beyssac, O., Catlos, E. J., Harrison, T. M., Grove, M., et al. (2004). Thermal structure and exhumation history of the Lesser Himalaya in central Nepal. *Tectonics*, *23*, TC5015. https://doi.org/10.1029/2003TC001564

Bollinger, L., Henry, P., & Avouac, J. P. (2006). Mountain building in the Nepal Himalaya: Thermal and kinematic model. *Earth and Planetary Science Letters*, *244*(1–2), 58–71. https://doi.org/10.1016/j.epsl.2006.01.045

Brewer, I. D., Burbank, D. W., & Hodges, K. V. (2003). Modelling detrital cooling-age populations: Insights from two Himalayan catchments. *Basin Research*, *15*(3), 305–320. https://doi.org/10.1046/j.1365-2117.2003.00211.x

Caddick, M. J., Bickle, M. J., Harris, N. B. W., Holland, T. J. B., Horstwood, M. S. A., Parrish, R. R., & Ahmad, T. (2007). Burial and exhumation history of a Lesser Himalayan schist: Recording the formation of an inverted metamorphic sequence in NW India. *Earth and Planetary Science Letters*, *264*(3-4), 375–390. https://doi.org/10.1016/j.epsl.2007.09.011

Carosi, R., Montomoli, C., & Iaccarino, S. (2018). 20 years of geological mapping of the metamorphic core across central and eastern Himalayas. *Earth-Science Reviews*, *177*, 124–138. https://doi.org/10.1016/j.earscirev.2017.11.006

Carosi, R., Montomoli, C., Rubatto, D., & Visona, D. (2013). Leucogranite intruding the South Tibetan Detachment in western Nepal: Implications for exhumation models in the Himalayas. *Terra Nova*, *25*(6), 478–489. https://doi.org/10.1111/ter.12062

Carosi, R., Musumeci, G., & Pertusati, P. C. (1999). Extensional tectonics in the higher Himalayan crystallines of Khumbu Himal, Eastern Nepal. In A. Macfarlane, R. B. Sorkhabai, & J. Quade (Eds.), *Himalaya and Tibet: Mountain roots to mountain tops*, (Vol. 328, pp. 211–223). Denver, CO: Geological Society of America Special Paper.

Catlos, E. J. (2000). Geochronologic and thermobarometric constraints on the evolution of the main central thrust, Himalayan orogen (PhD thesis). Los Angeles: University of California.

Catlos, E. J. (2013). Generalizations about monazite: Implications for geochronologic studies. *American Mineralogist*, *98*(5-6), 819–832. https://doi.org/10.2138/am.2013.4336

Catlos, E. J., Harrison, T. M., Kohn, M. J., Grove, M., Ryerson, F. J., Manning, C. E., & Upreti, B. N. (2001). Geochronologic and thermobarometric constraints on the evolution of the Main Central Thrust, central Nepal Himalaya. *Journal of Geophysical Research*, *106*(B8), 16,177–16,204. https://doi.org/10.1029/2000JB900375

Chakraborty, S., Anczkiewicz, R., Gaidies, F., Rubatto, D., Sorcar, N., Faak, K., et al. (2016). A review of thermal history and timescales of tectonometamorphic processes in Sikkim Himalaya (NE India) and implications for rates of metamorphic processes. *Journal of Metamorphic Geology*, *34*(8), 785–803. https://doi.org/10.1111/jmg.12200

Clarke, G. L., Bhowmik, S. K., Ireland, T. R., Aitchison, J. C., Chapman, S. L., & Kent, L. (2016). Inverted Oligo-Miocene metamorphism in the Lesser Himalaya sequence, Arunachal Pradesh, India: Age and grade relationships. *Journal of Metamorphic Geology*, *34*(8), 805–820. https://doi.org/10.1111/jmg.12202

Coggon, R., & Holland, T. J. B. (2002). Mixing properties of phengitic micas and revised garnet-phengite thermobarometers. *Journal of Metamorphic Geology*, *20*(7), 683–696. https://doi.org/10.1046/j.1525-1314.2002.00395.x

Coleman, M. E. (1998). U-Pb constraints on Oligocene-Miocene deformation and anatexis within the central Himalaya, Marsyangdi Valley, Nepal. *American Journal of Science*, *298*(7), 553–571. https://doi.org/10.2475/ajs.298.7.553

Corrie, S. L., & Kohn, M. J. (2011). Metamorphic history of the central Himalaya, Annapurna region, Nepal, and implications for tectonic models. *Bulletin of the Geological Society of America*, *123*(9–10), 1863–1879. https://doi.org/10.1130/B30376.1

Cottle, J. M., Larson, K. P., & Kellett, D. A. (2015). How does the mid-crust accommodate deformation in large, hot collisional orogens? A review of recent research in the Himalayan orogen. *Journal of Structural Geology*, *78*, 119–133. https://doi.org/10.1016/j.jsg.2015.06.008

Daniel, C. G., Hollister, L . S., Parrish, R. R., & Grujic, D. (2003). Exhumation of the Main Central Thrust from lower crustal depths, eastern Bhutan Himalaya. *Journal of Metamorphic Geology*, *21*(4), 317–334. https://doi.org/10.1046/j.1525-1314.2003.00445.x

DeCelles, P. G., Robinson, D. M., Quade, J., Ojha, T. P., Garzione, C. N., Copeland, P., & Upreti, B. N. (2001). Stratigraphy, structure, and tectonic evolution of the Himalayan fold-thrust belt in western Nepal. *Tectonics*, *20*, 487–509.

De Capitani, C., & Brown, T. H. (1987). The computation of chemical equilibrium in complex systems containing non-ideal solutions. *Geochimica et Cosmochimica Acta*, *51*(10), 2639–2652. https://doi.org/10.1016/0016-7037(87)90145-1

De Capitani, C., & Petrakakis, K. (2010). The computation of equilibrium assemblage diagrams with Theriak/Domino software. *American Mineralogist*, *95*(7), 1006–1016. https://doi.org/10.2138/am.2010.3354

Edwards, R. M. (1995). $^{40}Ar/^{39}Ar$ geochronology of the Main Central Thrust (MCT) region; evidence for late Miocene to Pliocene disturbances along the MCT, Marsyangdi River valley, west-central Nepal Himalaya. *Journal of Nepal Geological Society*, *10*, 41–46.

England, P. C., LeFort, P., Molnar, P., & Pêcher, A. (1992). Heat sources for Tertiary metamorphism and anatexis in the Annapurna-Manaslu region, central Nepal. *Journal of Geophysical Research*, *97*(B2), 2107–2128. https://doi.org/10.1029/91JB02272

England, P. C., & Molnar, P. (1993). The interpretation of inverted metamorphic isograds using simple physical calculations. *Tectonics*, *12*(1), 145–157. https://doi.org/10.1029/92TC00850

Evans, T. P. (2004). A method for calculating effective bulk composition modification due to crystal fractionation in garnet-bearing schist: Implications for isopleth thermobarometry. *Journal of Metamorphic Geology*, *22*(6), 547–557. https://doi.org/10.1111/j.1525-1314.2004.00532.x

Ferry, J. M., & Spear, F. S. (1978). Experimental calibration of partitioning of Fe and Mg between biotite and garnet. *Contributions to Mineralogy and Petrology*, *66*(2), 113–117. https://doi.org/10.1007/BF00372150

Foster, G., Kinny, P., Vance, D., Prince, C., & Harris, N. (2000). The significance of monazite U-Th-Pb age data in metamorphic assemblages; a combined study of monazite and garnet chronometry. *Earth and Planetary Science Letters*, *181*(3), 327–340. https://doi.org/10.1016/S0012-821X(00)00212-0

Fraser, G., Worley, B., & Sandiford, M. (2000). High-precision geothermobarometry across the high Himalayan metamorphic sequence, Langtang Valley, Nepal. *Journal of Metamorphic Geology*, *18*(6), 665–681. https://doi.org/10.1046/j.1525-1314.2000.00283.x

Gaidies, F., Petley-Ragan, A., Chakraborty, S., Dasgupta, S., & Jones, P. (2015). Constraining the conditions of barrovian metamorphism in Sikkim, India: P-T-t paths of garnet crystallization in the Lesser Himalayan Belt. *Journal of Metamorphic Geology*, *33*(1), 23–44. https://doi.org/10.1111/jmg.12108

George, F. R., & Gaidies, F. (2017). Characterisation of a garnet population from the Sikkim Himalaya: Insights into the rates and mechanisms of porphyroblast crystallization. *Contributions to Mineralogy and Petrology*, *172*(7). https://doi.org/10.1007/s00410-017-1372-y

Gervais, F., & Brown, R. L. (2011). Testing modes of exhumation in collisional orogens: Synconvergent channel flow in the southeastern Canadian Cordillera. *Lithosphere*, *3*(1), 55–75. https://doi.org/10.1130/L98.1

Goscombe, B., & Hand, M. (2000). Contrasting P-T paths in the eastern Himalaya, Nepal: Inverted isograds in a paired metamorphic mountain belt. *Journal of Petrology*, *41*(12), 1673–1719. https://doi.org/10.1093/petrology/41.12.1673

Goswami, S., Bhowmik, S. K., & Dasgupta, S. (2009). Petrology of a non-classical Barrovian inverted metamorphic sequence from the western Arunachal Himalaya, India. *Journal of Asian Earth Sciences*, *36*(4-5), 390–406. https://doi.org/10.1016/j.jseaes.2009.07.006

Goswami-Banerjee, S., Bhowmik, S. K., Dasgupta, S., & Pant, N. C. (2014). Burial of thermally perturbed Lesser Himalayan mid-crust: Evidence from petrochemistry and P-T estimation of the western Arunachal Himalaya, India. *Lithos*, *208-209*, 298–311. https://doi.org/10.1016/j.lithos.2014.09.015

Groppo, C., Rolfo, F., & Lombardo, B. (2009). P-T evolution across the Main Central Thrust Zone (eastern Nepal): Hidden discontinuities revealed by petrology. *Journal of Petrology*, *50*(6), 1149–1180. https://doi.org/10.1093/petrology/egp036

Groppo, C., Rubatto, D., Rolfo, F., & Lombardo, B. (2010). Early Oligocene partial melting in the Main Central Thrust Zone (Arun valley, eastern Nepal Himalaya). *Lithos*, *118*(3-4), 287–301. https://doi.org/10.1016/j.lithos.2010.05.003

Guillot, S. (1999). An overview of the metamorphic evolution in Central Nepal. *Journal of Asian Earth Sciences*, *17*(5-6), 713–725. https://doi.org/10.1016/S1367-9120(99)00045-0

Harrison, T. M., Grove, M., Lovera, O. M., & Catlos, E. J. (1998). A model for the origin of Himalayan anatexis and inverted metamorphism. *Journal of Geophysical Research*, *103*(B11), 27,017–27,032. https://doi.org/10.1029/98JB02468

Hauck, M. L., Nelson, K. D., Brown, L. D., Zhao, W., & Ross, A. R. (1998). Crustal structure of the Himalayan Orogen at approximately 90 degrees east longitude from Project INDEPTH deep reflection profiles. *Tectonics*, *17*, 481–500.

Henry, P., Le Pichon, X., & Goffe, B. (1997). Kinematic, thermal and petrological model of the Himalayas: Constraints related to metamorphism within the underthrust Indian crust and topographic elevation. *Tectonophysics*, *273*(1-2), 31–56. https://doi.org/10.1016/S0040-1951(96)00287-9

Herman, F., Copeland, P., Avouac, J. P., Bollinger, L., Mahéo, G., le Fort, P., et al. (2010). Exhumation, crustal deformation, and thermal structure of the Nepal Himalaya derived from the inversion of thermochronological and thermobarometric data and modeling of the topography. *Journal of Geophysical Research*, *115*, B06407. https://doi.org/10.1029/2008JB006126

Hodges, K., Bowring, S., Davidek, K., Hawkins, D., & Krol, M. (1998). Evidence for rapid displacement on Himalayan normal faults and the importance of tectonic denudation in the evolution of mountain ranges. *Geology*, *26*(6), 483–486. https://doi.org/10.1130/0091-7613(1998)026<0483:EFRDOH>2.3.CO;2

Hodges, K. V. (2006). A synthesis of the channel flow-extrusion hypothesis as developed for the Himalayan-Tibetan orogenic system. In R. D. Law, M. P. Searle, & L. Godin (Eds.), *Channel flow, ductile extrusion and exhumation in continental collision zones*, *Geological society special publication* (Vol. 268, pp. 71–90). London, UK: Geological Society.

Hodges, K. V., Le Fort, P., & Pecher, A. (1988). Possible thermal buffering by crustal anatexis in collisional orogens; thermobarometric evidence from the Nepalese Himalaya. *Geology*, *16*, 707–710.

Hodges, K. V., Parrish, R. R., & Searle, M. P. (1996). Tectonic evolution of the central Annapurna Range, Nepalese Himalayas. *Tectonics*, *15*(6), 1264–1291. https://doi.org/10.1029/96TC01791

Hoisch, T. D. (1990). Empirical calibration of six geobarometers for the mineral assemblage quartz + muscovite + biotite + plagioclase + garnet. *Contributions to Mineralogy and Petrology*, *104*(2), 225–234. https://doi.org/10.1007/BF00306445

Holdaway, M. J. (2004). Optimization of some key geothermobarometers for pelitic metamorphic rocks. *Mineralogical Magazine*, *68*(1), 1–14. https://doi.org/10.1180/0026461046810167

Holland, T. B., & Powell, R. (1998). An internally consistent thermodynamic data set for phases of petrological interest. *Journal of Metamorphic Geology*, *16*(3), 309–343.

Holland, T. J. B., Baker, J. M., & Powell, R. (1998). Mixing properties and activity—Composition relationships of chlorites in the system MgO-FeO-Al$_2$O$_3$-SiO$_2$-H$_2$O. *European Journal of Mineralogy*, *10*(3), 395–406. https://doi.org/10.1127/ejm/10/3/0395

Holland, T. J. B., & Powell, R. (2003). Activity-composition relations for phases in petrological calculations: An asymmetric multicomponent formulation. *Contributions to Mineralogy and Petrology*, *145*(4), 492–501. https://doi.org/10.1007/s00410-003-0464-z

Hubbard, M. S. (1989). Thermobarometric constraints on the thermal history of the Main Central Thrust Zone and Tibet Slab, eastern Nepal Himalaya. *Journal of Metamorphic Geology*, *7*(1), 19–30. https://doi.org/10.1111/j.1525-1314.1989.tb00572.x

Hubbard, M. S. (1996). Ductile shear as a cause of inverted metamorphism: Example from the Nepal Himalaya. *Journal of Geology*, *104*(4), 493–499. https://doi.org/10.1086/629842

Iaccarino, S., Montomoli, C., Carosi, R., Massonne, H.-J., & Visonà, D. (2017). Geology and tectono-metamorphic evolution of the Himalayan metamorphic core: Insights from the Mugu Karnali transect, western Nepal (central Himalaya). *Journal of Metamorphic Geology*, *35*(3), 301–325, doi. https://doi.org/10.1111/jmg.12233

Imayama, T., Takeshita, T., & Arita, K. (2010). Metamorphic P-T profile and P-T path discontinuity across the far-eastern Nepal Himalaya: Investigation of channel flow models. *Journal of Metamorphic Geology*, *28*(5), 527–549. https://doi.org/10.1111/j.1525-1314.2010.00879.x

Imayama, T., Takeshita, T., Yi, K., Cho, D.-L., Kitajima, K., Tsutsumi, Y., et al. (2012). Two-stage partial melting and contrasting cooling history within the Higher Himalayan Crystalline Sequence in the far-eastern Nepal Himalaya. *Lithos*, *134-135*, 1–22. https://doi.org/10.1016/j.lithos.2011.12.004

Inger, S., & Harris, N. B. W. (1992). Tectonothermal evolution of the High Himalaya Crystalline sequence, Langtang Valley, northern Nepal. *Journal of Metamorphic Geology*, *10*(3), 439–452. https://doi.org/10.1111/j.1525-1314.1992.tb00095.x

Kaneko, Y. (1995). Thermal structure in the Annapurna region, central Nepal Himalaya; implication for the inverted metamorphism. *Journal of Mineralogy, Petrology and Economic Geology*, *90*, 143–154.

Kohn, M. J. (2008). P-T-t data from central Nepal support critical taper and repudiate large-scale channel flow of the Greater Himalayan Sequence. *Geological Society of America Bulletin*, *120*(3-4), 259–273. https://doi.org/10.1130/B26252.1

Kohn, M. J. (2014a). "Thermoba-Raman-try": Calibration of spectroscopic barometers and thermometers for mineral inclusions. *Earth and Planetary Science Letters*, *388*, 187–196. https://doi.org/10.1016/j.epsl.2013.11.054

Kohn, M. J. (2014b). Himalayan metamorphism and its tectonic implications. *Annual Review of Earth and Planetary Sciences*, *42*(1), 381–419. https://doi.org/10.1146/annurev-earth-060313-055005

Kohn, M. J. (2016). Metamorphic chronology—A tool for all ages: Past achievements and future prospects. *American Mineralogist*, *101*(1), 25–42. https://doi.org/10.2138/am-2016-5146

Kohn, M. J., Catlos, E. J., Ryerson, F. J., & Harrison, T. M. (2001). Pressure-temperature-time path discontinuity in the Main Central thrust zone, central Nepal. *Geology*, *29*, 571–574.

Kohn, M. J., & Spear, F. (2000). Retrograde net transfer reaction insurance for pressure-temperature estimates. *Geology*, *28*(12), 1127–1130. https://doi.org/10.1130/0091-7613(2000)28<1127:RNTRIF>2.0.CO;2

Kohn, M. J., Wieland, M. S., Parkinson, C. D., & Upreti, B. N. (2004). Miocene faulting at plate tectonic velocity in the Himalaya of central Nepal. *Earth and Planetary Science Letters*, *228*(3-4), 299–310. https://doi.org/10.1016/j.epsl.2004.10.007

Kohn, M. J., Wieland, M. S., Parkinson, C. D., & Upreti, B. N. (2005). Five generations of monazite in Langtang gneisses: Implications for chronology of the Himalayan metamorphic core. *Journal of Metamorphic Geology*, *23*(5), 399–406. https://doi.org/10.1111/j.1525-1314.2005.00584.x

Landry, K. R., Coutand, I., Whipp, D. M. Jr., Grujic, D., & Hourigan, J. K. (2016). Late Neogene tectonically driven crustal exhumation of the Sikkim Himalaya: Insights from inversion of multithermochronologic data. *Tectonics*, *35*, 833–859. https://doi.org/10.1002/2015TC004102

Lang, K. A., Huntington, K. W., Burmester, R. F., & Housen, B. (2016). Rapid exhumation of the eastern Himalayan syntaxis since the late Miocene. *Geological Society of America Bulletin*, *128*(9-10), 1403–1422. https://doi.org/10.1130/B31419.1

Larson, K. P., Ambrose, T. K., Webb, A. G., Cottle, J. M., & Shrestha, S. (2015). Reconciling Himalayan midcrustal discontinuities: The Main Central Thrust system. *Earth and Planetary Science Letters*, *429*, 139–146. https://doi.org/10.1016/j.epsl.2015.07.070

Larson, K. P., Camacho, A., Cottle, J. M., Coutand, I., Buckingham, H. M., Ambrose, T. K., & Rai, S. M. (2017). Cooling, exhumation, and kinematics of the Kanchenjunga Himal, far east Nepal. *Tectonics*, *36*, 1037–1052. https://doi.org/10.1002/2017TC004496

Larson, K. P., Gervais, F., & Kellett, D. A. (2013). A P–T–t–D discontinuity in east-central Nepal: Implications for the evolution of the Himalayan mid-crust. *Lithos*, *179*, 275–292. https://doi.org/10.1016/j.lithos.2013.08.012

LeFort, P. (1975). Himalaya, the collided range, present knowledge of the continental arc. *American Journal of Science*, *275A*, 1–44.

Lombardo, B., & Rolfo, F. (2000). Two contrasting eclogite types in the Himalayas: Implications for the Himalayan orogeny. *Journal of Geodynamics*, *30*(1-2), 37–60. https://doi.org/10.1016/S0264-3707(99)00026-5

Long, S., & McQuarrie, N. (2010). Placing limits on channel flow: Insights from the Bhutan Himalaya. *Earth and Planetary Science Letters*, *290*(3-4), 375–390. https://doi.org/10.1016/j.epsl.2009.12.033

Macfarlane, A. M. (1995). An evaluation of the inverted metamorphic gradient at Langtang National Park, central Nepal Himalaya. *Journal of Metamorphic Geology*, *13*(5), 595–612. https://doi.org/10.1111/j.1525-1314.1995.tb00245.x

Mahar, E. M., Baker, J. M., Powell, R., Holland, T. J. B., & Howell, N. (1997). The effect of Mn on mineral stability in metapelites. *Journal of Metamorphic Geology*, *15*(2), 223–238. https://doi.org/10.1111/j.1525-1314.1997.00011.x

Manickavasagam, R. M., Jain, A. K., Singh, S., & Asokan, A. (1999). Metamorphic evolution of the northwest Himalaya, India: Pressure-temperature data, inverted metamorphism, and exhumation in the Kashmir, Himachal, and Garhwal Himalayas. In A. Macfarlane, R. B. Sorkhabai, & J. Quade (Eds.), *Himalaya and Tibet: Mountain roots to mountain tops* (Vol. 328, pp. 179–198). Denver, CO: Geological Society of America Special Paper.

Martin, A. J. (2017). A review of definitions of the Himalayan Main Central Thrust. *International Journal of Earth Sciences*, *106*(6), 2131–2145. https://doi.org/10.1007/s00531-016-1419-8

Martin, A. J., Copeland, P., & Benowitz, J. A. (2014). Muscovite ^{40}Ar/^{39}Ar ages help reveal the Neogene tectonic evolution of the southern Annapurna Range, central Nepal. *Geological Society, London, Special Publications*, *412*(1), 199–220. https://doi.org/10.1144/SP412.5

Martin, A. J., Ganguly, J., & DeCelles, P. G. (2010). Metamorphism of Greater And Lesser Himalayan rocks exposed in the Modi Khola valley, central Nepal. *Contributions to Mineralogy and Petrology*, *159*(2), 203–223. https://doi.org/10.1007/s00410-009-0424-3

Mattinson, C. G., Regel, M. E., & Zhang, J. (2014). Comparison of conventional, trace element, and pseudosection thermobarometry in UHP eclogite, North Qaidam terrane, western China. Paper presented at the American Geophysical Union, Fall Meeting, San Francisco, CA, Abstract #V31D-4788.

Metcalfe, R. P. (1993). Pressure, temperature and time constraints on metamorphism across the Main Central Thrust zone and High Himalaya Slab in the Garhwal Himalaya. In P. J. Trealor, & M. P. Searle (Eds.), *Himalayan tectonics* (Vol. 74, pp. 485–509). London, UK: Geological Society Special Publication.

Moharana, A., Mishra, A., & Srivastava, D. C. (2013). Deformation style in the Munsiari Thrust Zone: A study in the Madlakia–Munsiari–Dhapa section in north-eastern Kumaun Himalaya. *International Journal of Earth Sciences*, *102*(7), 1837–1849. https://doi.org/10.1007/s00531-013-0892-6

Montel, J. M., Kornprobst, J., & Vielzeuf, D. (2000). Preservation of old U-Th-Pb ages in shielded monazite: Example from the Benmi Bousera Hercynian kinzigites (Morocco). *Journal of Metamorphic Geology*, *18*, 335–342.

Montomoli, C., Iaccarino, S., Carosi, R., Langone, A., & Visona, D. (2013). Tectonometamorphic discontinuities within the Greater Himalayan Sequence in western Nepal (central Himalaya): Insights on the exhumation of crystalline rocks. *Tectonophysics*, *608*, 1349–1370. https://doi.org/10.1016/j.tecto.2013.06.006

Mosca, P., Groppo, C., & Rolfo, F. (2012). Structural and metamorphic features of the Main Central Thrust Zone and its contiguous domains in the eastern Nepalese Himalaya. In M. Zucali, M. I. Spalla, & G. Gosso (Eds.), *Multiscale structures and tectonic trajectories in active margins*, *Journal of the Virtual Explorer* (Vol. 41, pp. 1–34). Clayton, Victoria, Australia: Australian Crustal Research Centre, Monash University. https://doi.org/10.3809/jvirtex.2011.00294

Mottram, C. M., Argles, T. W., Harris, N. B. W., Parrish, R. R., Horstwood, M. S. A., Warren, C. J., & Gupta, S. (2014). Tectonic interleaving along the Main Central Thrust, Sikkim Himalaya. *Journal of the Geological Society of London*, *171*(2), 255–268. https://doi.org/10.1144/jgs2013-064

Mottram, C. M., Parrish, R. R., Regis, D., Warren, C. J., Argles, T. W., Harris, N. B. W., & Roberts, N. M. W. (2015). Using U-Th-Pb petrochronology to determine rates of ductile thrusting: Time windows into the Main Central Thrust, Sikkim Himalaya. *Tectonics*, *34*, 1355–1374. https://doi.org/10.1002/2014TC003743

Mottram, C. M., Warren, C. J., Regis, D., Roberts, N. M. W., Harris, N. B. W., Argles, T. W., & Parrish, R. R. (2014). Developing an inverted Barrovian sequence: Insights from monazite petrochronology. *Earth and Planetary Science Letters*, *403*, 418–431. https://doi.org/10.1016/j.epsl.2014.07.006

Moynihan, D. P., & Pattison, D. R. M. (2013). An automated method for the calculation of P-T paths from garnet zoning, with application to metapelitic schist from the Kootenay Arc, British Columbia, Canada. *Journal of Metamorphic Geology*, *31*(5), 525–548. https://doi.org/10.1111/jmg.12032

Mukhopadhyay, D. K., Chakraborty, S., Trepmann, C., Rubatto, D., Anczkiewicz, R., Gaidies, F., et al. (2017). The nature and evolution of the Main Central Thrust: Structural and geochronological constraints from the Sikkim Himalaya, NE India. *Lithos*, *282–283*, 447–463. https://doi.org/10.1016/j.lithos.2017.01.015

Nandini, P., & Thakur, S. S. (2011). Metamorphic evolution of the Lesser Himalayan crystalline sequence, Siyom Valley, NE Himalaya, India. *Journal of Asian Earth Sciences*, *40*(5), 1089–1100. https://doi.org/10.1016/j.jseaes.2010.12.005

Palin, R. M., Weller, O. M., Waters, D. J., & Dyck, B. (2016). Quantifying geological uncertainty in metamorphic phase equilibria modelling: A Monte Carlo assessment and implications for tectonic interpretations. *Geoscience Frontiers*, *7*, 591–607. https://doi.org/10.1016/j.gsf.2015.08.005

Parsons, A. J., Law, R. D., Lloyd, G. E., Phillips, R. J., & Searle, M. P. (2016). Thermo-kinematic evolution of the Annapurna-Dhaulagiri Himalaya, central Nepal: The Composite Orogenic System. *Geochemistry, Geophysics, Geosystems*, *17*, 1511–1539. https://doi.org/10.1002/2015GC006184

Pêcher, A. (1989). The metamorphism in the central Himalaya. *Journal of Metamorphic Geology*, *7*(1), 31–41. https://doi.org/10.1111/j.1525-1314.1989.tb00573.x

Plumhoff, A. M., & Spear, F. S. (2016). Application of quig barometry to the Barrovian zones, Scotland: A re-evaluation of classical geobarometry in a classic locality. Paper presented at the Geological Society of America, northeastern section, 51st annual meeting. https://doi.org/10.1130/abs/2016NE-272650

Pognante, U., & Benna, P. (1993). Metamorphic zonation, migmitization and leucogranites along the Everest transect of eastern Nepal and Tibet: Record of an exhumation history. In P. J. Trealor, & M. P. Searle (Eds.), *Himalayan tectonics* (Vol. 74, pp. 323–340). London, UK: Geological Society Special Publication.

Powell, R., & Holland, T. J. B. (1999). Relating formulations of the thermodynamics of mineral solid solutions: Activity modeling of pyroxenes, amphiboles, and micas. *American Mineralogist*, *84*(1-2), 1–14. https://doi.org/10.2138/am-1999-1-201

Rapa, G., Groppo, C., Mosca, P., & Rolfo, F. (2016). Petrological constraints on the tectonic setting of the Kathmandu Nappe in the Langtang-Gosainkund-Helambu regions, central Nepal Himalaya. *Journal of Metamorphic Geology*, *34*(9), 999–1023. https://doi.org/10.1111/jmg.12219

Rasmussen, B., & Muhling, J. R. (2007). Monazite begets monazite: Evidence for dissolution of detrital monazite and reprecipitation of syn-tectonic monazite during low-grade regional metamorphism. *Contributions to Mineralogy and Petrology*, *154*(6), 675–689. https://doi.org/10.1007/s00410-007-0216-6

Robinson, D. M., & Martin, A. J. (2014). Reconstructing the greater Indian margin; a balanced cross section in central Nepal focusing on the Lesser Himalayan duplex. *Tectonics*, *33*, 2143–2168. https://doi.org/10.1002/2014TC003564

Rolfo, F., Groppo, C., & Mosca, P. (2014). Petrological constraints of the "Channel Flow" model in eastern Nepal. *Geological Society, London, Special Publications*, *412*(1), 177–197. https://doi.org/10.1144/SP412.4

Ruhl, K. W., & Hodges, K. V. (2005). The use of detrital mineral cooling ages to evaluate steady state assumptions in active orogens: An example from the central Nepalese Himalaya. *Tectonics*, *24*, TC4015. https://doi.org/10.1029/2004TC001712

Schmalholz, S. M., & Podladchikov, Y. Y. (2013). Tectonic overpressure in weak crustal-scale shear zones and implications for the exhumation of high-pressure rocks. *Geophysical Research Letters*, *40*, 1984–1988. https://doi.org/10.1002/grl.50417

Searle, M. P., Law, R. D., Godin, L., Larson, K. P., Streule, M. J., Cottle, J. M., & Jessup, M. J. (2008). Defining the Himalayan Main Central Thrust in Nepal. *Journal of the Geological Society of London*, *165*(2), 523–534. https://doi.org/10.1144/0016-76492007-081

Searle, M. P., & Rex, A. J. (1989). Thermal model for the Zanskar Himalaya. *Journal of Metamorphic Geology*, *7*(1), 127–134. https://doi.org/10.1111/j.1525-1314.1989.tb00579.x

Spear, F. S. (1993). *Metamorphic phase equilibria and pressure-temperature-time paths* (p. 799). Washington, D.C.: Mineralogical Society of America.

Spear, F. S., Kohn, M. J., Florence, F. P., & Menard, T. (1990). A model for garnet and plagioclase growth in pelitic schists: Implications for thermobarometry and P-T path determinations. *Journal of Metamorphic Geology*, *8*(6), 683–696. https://doi.org/10.1111/j.1525-1314.1990.tb00495.x

Spear, F. S., & Selverstone, J. (1983). Quantitative P-T paths from zoned minerals: Theory and tectonic applications. *Contributions to Mineralogy and Petrology*, *83*(3-4), 348–357. https://doi.org/10.1007/BF00371203

Spear, F. S., Thomas, J. B., & Hallett, B. W. (2014). Overstepping the garnet isograd: A comparison of QuiG barometry and thermodynamic modeling. *Contributions to Mineralogy and Petrology*, *168*(3), 1–15. https://doi.org/10.1007/s00410-014-1059-6

Staeubli, A. (1989). Polyphase metamorphism and the development of the Main Central Thrust. *Journal of Metamorphic Geology*, *7*(1), 73–93. https://doi.org/10.1111/j.1525-1314.1989.tb00576.x

Stephenson, B. J., Waters, D. J., & Searle, M. P. (2000). Inverted metamorphism and the Main Central Thrust: Field relations and thermo-barometric constraints from the Kishtwar Window, NW Indian Himalaya. *Journal of Metamorphic Geology*, *18*(5), 571–590. https://doi.org/10.1046/j.1525-1314.2000.00277.x

Szulc, A. G., Najman, Y., Sinclair, H., Pringle, M., Bickle, M., Chapman, H., et al. (2006). Tectonic evolution of the Himalaya constrained by detrital [40]Ar–[39]Ar, Sm–Nd and petrographic data from the Siwalik foreland basin succession, SW Nepal. *Basin Research*, *18*(4), 375–391. https://doi.org/10.1111/j.1365-2117.2006.00307.x

Thakur, S. S., Patel, S. C., & Singh, A. K. (2015). A P-T pseudosection modelling approach to understand metamorphic evolution of the Main Central Thrust zone in the Alaknanda Valley, NW Himalaya. *Contributions to Mineralogy and Petrology*, *170*(1). https://doi.org/10.1007/s00410-015-1159-y

Tinkham, D. K., & Ghent, E. D. (2005). Estimating P-T conditions of garnet growth with isochemical phase-diagram sections and the problem of effective bulk-composition. *Canadian Mineralogist*, *43*(1), 35–50. https://doi.org/10.2113/gscanmin.43.1.35

Tobgay, T., McQuarrie, N., Long, S., Kohn, M. J., & Corrie, S. L. (2012). The age and rate of displacement along the Main Central Thrust in the western Bhutan Himalaya. *Earth and Planetary Science Letters*, *319-320*, 146–158. https://doi.org/10.1016/j.epsl.2011.12.005

Upreti, B. N. (1999). An overview of the stratigraphy and tectonics of the Nepal Himalaya. *Journal of Asian Earth Sciences*, *17*, 741–753. https://doi.org/10.1016/S1367-9120(99)00047-4

Vannay, J.-C., & Grasemann, B. (1998). Inverted metamorphism in the High Himalaya of Himachal Pradesh (NW India): Phase equilibria versus thermobarometry. *Schweizerische Mineralogische und Petrographische Mitteilungen*, *78*, 107–132.

Vannay, J.-C., & Hodges, K. V. (1996). Tectonometamorphic evolution of the Himalayan metamorphic core between Annapurna and Dhaulagiri, central Nepal. *Journal of Metamorphic Geology*, *14*, 635–656.

Walters, J. B., & Kohn, M. J. (2017). Protracted thrusting followed by late rapid cooling of the Greater Himalayan Sequence, Annapurna Himalaya, Central Nepal: Insights from titanite petrochronology. *Journal of Metamorphic Geology*, *35*(8), 897–917. https://doi.org/10.1111/jmg.12260

Wang, J.-M., Zhang, J.-J., Liu, K., Zhang, B., Wang, X.-X., Rai, S., & Scheltens, M. (2016). Spatial and temporal evolution of tectonometamorphic discontinuities in the central Himalaya: Constraints from P-T paths and geochronology. *Tectonophysics*, *679*, 41–60. https://doi.org/10.1016/j.tecto.2016.04.035

White, N. M., Pringle, M., Garzanti, E., Bickle, M., Najman, Y., Chapman, H., & Friend, P. (2002). Constraints on the exhumation and erosion of the High Himalayan Slab, NW India, from foreland basin deposits. *Earth and Planetary Science Letters*, *195*(1-2), 29–44. https://doi.org/10.1016/S0012-821X(01)00565-9

White, R. W., Pomroy, N. E., & Powell, R. (2005). An in situ metatexite-diatexite transition in upper amphibolite facies rocks from Broken Hill, Australia. *Journal of Metamorphic Geology*, *23*(7), 579–602. https://doi.org/10.1111/j.1525-1314.2005.00597.x

White, R. W., Powell, R., Holland, T. J. B., & Worley, B. A. (2000). The effect of TiO_2 and Fe_2O_3 on metapelitic assemblages at greenschist and amphibolite facies conditions: Mineral equilibria calculations in the system K_2O-FeO-MgO-Al_2O_3-SiO_2- H_2O-TiO_2-Fe_2O_3. *Journal of Metamorphic Geology*, *18*(5), 497–511. https://doi.org/10.1046/j.1525-1314.2000.00269.x

Wolfe, O. M., & Spear, F. S. (2015a). Comparison of Quig barometry with conventional thermobarometry in the Townshend-Browning Syncline, Vermont. Paper presented at the Geological Society of America, Northeastern Section, 50th annual meeting, v. 47, 131. https://gsa.confex.com/gsa/2015NE/finalprogram/abstract_252553.htm

Wolfe, O. M., & Spear, F. S. (2015b). Constraints on tectonic burial from QuiG barometry, Connecticut Valley synclinorium, central Vermont. Paper presented at the Geological Society of America annual meeting & exposition, v. 47, 770. https://gsa.confex.com/gsa/2015AM/webprogram/Paper267877.html

Wolfe, O. M., & Spear, F. S. (2016). Thermobarometric comparison across the Richardson Memorial Contact, Bethel, Vermont. Paper presented at the Geological Society of America, northeastern section, 51st Annual Meeting, https://doi.org/10.1130/abs/2016NE-272587

Yin, A. (2006). Cenozoic tectonic evolution of the Himalayan orogen as constrained by along-strike variation of structural geometry, exhumation history, and foreland sedimentation. *Earth-Science Reviews*, *76*(1-2), 1–131. https://doi.org/10.1016/j.earscirev.2005.05.004

Zeh, A., & Holness, M. B. (2003). The effect of reaction overstep on garnet microtextures in metapelitic rocks of the Ilesha Schist Belt, SW Nigeria. *Journal of Petrology*, *44*(6), 967–994. https://doi.org/10.1093/petrology/44.6.967